An improved carbon greenhouse gas simulation in GEOS-Chem version 12.1.1

Beata Bukosa[1,2], Jenny A. Fisher[2], Nicholas M. Deutscher[2], and Dylan B. A. Jones[3]

[1]National Institute of Water and Atmospheric Research, Wellington, New Zealand
[2]Centre for Atmospheric Chemistry, School of Earth, Atmospheric and Life Sciences, Faculty of Science, Medicine and Health, University of Wollongong, NSW, Australia
[3]Department of Physics, University of Toronto, Toronto, ON, Canada

Correspondence: Beata Bukosa (beata.bukosa@niwa.co.nz)

Abstract. Understanding greenhouse gas–climate processes and feedbacks is a fundamental step in understanding climate variability and its links to greenhouse gas fluxes. Chemical transport models are the primary tool for linking greenhouse gas fluxes to their atmospheric abundances. Hence accurate simulations of greenhouse gases are essential. Here, we present a new simulation in the GEOS-Chem chemical transport model that couples the two main greenhouse gases: carbon dioxide

5 (CO_2) and methane (CH_4), along with the indirect effects of carbon monoxide (CO), based on their chemistry. Our updates include the online calculation of the chemical production of CO from CH_4 and the online production of CO_2 from CO, both of which were handled offline in the previous versions of these simulations. We discuss differences between the offline (uncoupled) and online (coupled) calculation of the chemical terms and perform a sensitivity simulation to identify the impact of OH on the results. We compare our results with surface measurements from the NOAA Global Greenhouse Gas Reference

10 Network (NOAA GGGRN), total column measurements from the Total Carbon Column Observing Network (TCCON) and aircraft measurements from the Atmospheric Tomography Mission (ATom). Relative to the standard uncoupled simulation, our coupled results show better agreement with measurements. We use the remaining measurement-model differences to identify sources and sinks that are over or underestimated in the model. We find underestimated OH fields when calculating the CH_4 loss and CO production from CH_4. Biomass burning emissions and secondary production are underestimated for CO in the

15 Southern Hemisphere and we find enhanced anthropogenic sources in the Northern Hemisphere. We also find significantly stronger chemical production of CO_2 in tropical land regions, especially in the Amazon. The model-measurement differences also highlight biases in the calculation of CH_4 in the stratosphere and in vertical mixing that impacts all three gases.

1 Introduction

Accurate simulations of greenhouse gases are vital for climate predictions. Carbon dioxide (CO_2) and methane (CH_4) are the

20 two main anthropogenic greenhouse gases and have significant impact on our climate. Due to human activities, the atmospheric amounts of CO_2 and CH_4 have increased globally by 40% and 150%, respectively, since the industrial revolution (Stocker et al., 2014). Carbon monoxide (CO) is less abundant than CO_2 and CH_4; however, through its indirect effect on CH_4, ozone and CO_2 it can also have a climate impact (Shindell et al., 2005). Changes in the atmospheric amounts of these gases, driven by

changes of their sources and sinks, largely control our future climate, but uncertainties about these processes and their budgets

25 still remain (Bousquet et al., 2006; Duncan et al., 2007; Liu et al., 2017). All three carbon greenhouse gases are chemically dependent, and a change in one can have a great effect on the other.

In the GEOS-Chem model, widely used for carbon gas flux inversion and source attribution, each of these gases have their own stand-alone simulation, decoupled from one another. Previous studies have emphasized the importance of the inclusion of the 3-D chemical production of CO_2 from the collective oxidation of CO, CH_4 and non-methane volatile organic compounds

30 (NMVOCs) (Enting and Mansbridge, 1991; Suntharalingam et al., 2005), but this chemical production, together with the secondary production of CO from CH_4, is handled offline in the stand-alone carbon gas simulations of the GEOS-Chem model (Nassar et al., 2010; Wecht et al., 2014; Fisher et al., 2017). Here, we present a new simulation in GEOS-Chem that couples CO_2, CH_4 and CO, with an online calculation of their chemical production for a more accurate simulation of these gases.

35 The majority of CH_4, the second most important anthropogenic greenhouse gas, is removed from the troposphere through reaction with OH:

$$CH_4 + OH \rightarrow CH_3 + H_2O \tag{R1}$$

that eventually leads to the formation of CO after a series of intermediate steps (Jacob, 1999):

$$CHO + O_2 \rightarrow CO + HO_2 \tag{R2}$$

40 Both CH_4 and CO have a common sink in the atmosphere through reaction with OH. The role of CO in determining tropospheric OH indirectly affects the atmospheric burden of CH_4 (Isaksen and Hov, 1987). It is one of the principal sinks of OH along with CH_4. Through reaction with OH, CO can also lead to the chemical formation of CO_2 (Enting and Mansbridge, 1991; Suntharalingam et al., 2005):

$$CO + OH \rightarrow CO_2 + H \tag{R3}$$

45 Oxidation of both primary CO, from direct anthropogenic and biomass burning emissions, and secondary CO, as an intermediate in the oxidation of CH_4 and NMVOCs, leads to the formation of CO_2. CO_2 can also be produced from the oxidation of carboxy–peroxy radical (RCO_3) and alkenoid ozonolysis (reaction of ethene with ozone; $C_2H_4+O_3$) (Folberth et al., 2005), but this is assumed to be only a minor contributor.

Aside from anthropogenic sources and outside source regions, the major source of CO is CH_4 oxidation by OH through

50 Reactions (R1) and (R2) and the intermediate reactions. Early studies found the yield of CO from CH_4 oxidation ranging from 0.70–1 (Logan et al., 1981; Tie et al., 1992; Manning et al.; Novelli et al., 1999; Bergamaschi et al., 2000; Duncan et al., 2007). The CO chemical production term is estimated to be 760–1086 Tg CO yr^{-1} (Holloway et al., 2000; Bergamaschi et al., 2000; Arellano Jr. and Hess, 2006; Duncan et al., 2007; Zeng et al., 2015; Fisher et al., 2017) and represents more than half of the total CO source.

55 The reaction of CO with OH radicals represents its largest sink, removing 2478–2630 Tg CO yr^{-1} (Bergamaschi et al., 2000; Pétron et al., 2004; Arellano Jr. and Hess, 2006; Nassar et al., 2010; Fisher et al., 2017). The total chemical CO_2 source

is estimated to be around 1.04–1.1 Pg C yr^{-1} (Suntharalingam et al., 2005; Nassar et al., 2010), which is about 12% of the annual anthropogenic CO_2 source (9.4 Pg C yr^{-1}, averaged for 2008–2017) (Le Quéré et al., 2018). Around 90–94% of the CO_2 chemical production is from CO oxidation (Folberth et al., 2005; Ciais et al., 2008). In contrast to the majority of the

60   CO_2 sources that are emitted at the surface, CO_2 from oxidation of CO is produced throughout the atmosphere. Although significant efforts have been made to constrain the total budgets of CO_2, CH_4 and CO, discrepancies in the chemical terms between studies suggest that these terms are still subject to uncertainties that can impact our understanding of the total budgets.

In this study, we introduce a new simulation in the GEOS-Chem model that couples the chemistry of three carbon greenhouse gases, CO_2, CH_4 and CO. With the new coupled simulation, our update eliminates the previously offline handling of the

65   chemical production between these gases (Nassar et al., 2010; Fisher et al., 2017), enabling us to have (i) better estimates of the chemical terms and (ii) simultaneous and consistent simulations of CO_2, CH_4 and CO that can help when constraining their fluxes based on their covariation (Wang et al., 2009; Pandey et al., 2015; Bukosa et al., 2019). Moreover, the coupled simulation removes the need to run the individual simulations separately if interested in all three gases, and it requires fewer computational resources than running three independent simulations.

70   We first describe the method for the online calculation of the chemical production, and the difference between the uncoupled and coupled versions of these simulations (Sect. 2). We then compare the stand-alone simulations of all three gases with the coupled simulation. For both versions we analyse their annual budgets and the contribution of chemical production to the total amount of each gas (Sect. 3 and 4) as well as their global spatial and temporal variability (Sect. 5). Finally, we validate the new coupled simulations against global surface flask measurements at sites part of the NOAA Global Greenhouse Gas Reference

75   Network (NOAA GGGRN), column measurements from the Total Carbon Column Observing Network (TCCON) and aircraft in situ measurements from the Atmospheric Tomography Mission (ATom) (Sect. 6).

2   GEOS-Chem

The coupled CO_2, CH_4 and CO simulation is based on version 12.1.1 of the GEOS-Chem 3-D global chemical transport model. The meteorological inputs for GEOS-Chem come from the Modern-Era Retrospective analysis for Research and Applications,

80   Version 2 (MERRA2) reanalysis developed by the NASA Global Modelling and Assimilation Office (GMAO). The native horizontal resolution of MERRA2 is 0.5°x0.625°. We ran the simulations at 2°x2.5° horizontal resolution with 47 vertical levels from January 2005 through December 2017. We used 10 min as the transport and convection timestep and 20 min for the chemistry and emissions timestep. Both the uncoupled and coupled simulations were initialized with a 10 year spinup for CO_2 and CH_4 using 2005 as a base spinup year, while for CO the model was spun up for 6 months in 2005. The spinup was carried

85   out with the uncoupled v11-01 simulations described in Bukosa et al. (2019). Due to differences between emission inventories used in Bukosa et al. (2019) and here, we use the first simulation year (2005) as an additional spinup year for all three gases. The production and loss terms used by each simulation are shown in Table 1 with additional common emission fields in the Supplement, Table S1. For simulation periods that are outside of the specified inventory time range, the model re-used the data from the closest year.

Table 1. GEOS-Chem production (P) and loss (L) terms used for the uncoupled and coupled carbon gas simulations.

	CO_2	CH_4	CO
Fields used by both uncoupled and coupled simulations			
Tropospheric OH sink	-	Archived fields[a,b,c]	Archived fields[c]
Stratospheric CH_4 loss	-	Archived fields[d]	-
Stratospheric CO	-	-	GMI[e]
$P(CO)_{NMVOC}$	-	-	$P(CO)_{NMVOC} = P(CO) - P(CO)_{CH_4}$
	-	-	offline, full chemistry[c]
Uncoupled only			
$L(CH_4)$	-	-	full chemistry
Time resolution	-	-	*Monthly mean, 2009–2011 average*
$P(CO)_{CH_4}$	-	-	offline, $P(CO)_{CH_4} = L(CH_4)$
Time resolution	-	-	*Monthly mean, 2009–2011 average*
$L(CO)$	full chemistry	-	-
Time resolution	*Monthly mean, 2004–2009*	-	-
$P(CO_2)$	offline, $P(CO_2) = L(CO)$	-	-
Time resolution	*Monthly mean, 2004–2009*	-	-
Coupled only			
$L(CH_4)$	-	-	online, from CH_4
Time resolution	-	-	*Every model timestep, 20 min*
$P(CO)_{CH_4}$	-	-	online, $P(CO)_{CH_4} = L(CH_4)$
Time resolution	-	-	*Every model timestep, 20 min*
$L(CO)$	online, from CO	-	-
Time resolution	*Every model timestep, 20 min*	-	-
$P(CO_2)$	online, $P(CO_2) = L(CO)$	-	-
Time resolution	*Every model timestep, 20 min*	-	

[a] We use two types of OH fields for the calculation of the CH_4 loss via OH as part of a sensitivity test described in Sect. 2.3., [b] Park et al., [c] Fisher et al. (2017), [d] Murray et al. (2012), [e] NASA Global Modeling Initiative model

2.1 Uncoupled GEOS-Chem simulations

The existing uncoupled simulations are based on Nassar et al. (2010) and Nassar et al. (2013) for CO_2, Wecht et al. (2014) and Maasakkers et al. (2019) for CH_4 and Fisher et al. (2017) for CO.

These simulations are decoupled from other gases, hence they require input fields including chemical production rates and OH losses. GEOS-Chem can also perform a full chemistry simulation, known as the *coupled aerosol–oxidant chemistry in the*

95 *troposphere and stratosphere* simulation. The full chemistry simulation is required for the functionality of some of the stand-alone simulations because it provides input fields for those simulations. Various versions of the full chemistry simulation have been run previously to archive the production rates and oxidant fields used in the carbon gas simulations. Both the production and oxidant fields are computed using 3-D archives of monthly average values. All three carbon greenhouse gas simulations are linear, and each includes a suite of tracers tagged by source type and/or region.

100   The stand-alone CH_4 simulation in the troposphere is based on Eq. (1):

$$\frac{d[CH_{4Trop}]}{dt} = E_{CH_4} - S_{CH_4} - k_{CH_4,OH}[OH][CH_4] - \\ - k_{CH_4,Cl}[Cl][CH_4]$$
(1)

where E_{CH_4} represents the surface emissions (gas, oil, coal, livestock, landfills, wastewater, biofuel, rice, biomass burning, wetlands, seeps, termites and other anthropogenic emissions), S_{CH_4} is the sink from soil absorption, $[OH]$, $[Cl]$ and $[CH_4]$ are
105   the atmospheric concentrations of OH, Cl and CH_4, and $k_{CH_4,OH}$ and $k_{CH_4,Cl}$ are the pressure- and temperature-dependent rate constants for oxidation of CH_4 by OH and Cl, respectively. In the stratosphere, Eq. (1) becomes:

$$\frac{d[CH_{4Strat}]}{dt} = E_{CH_4} - CH_{4loss}$$
(2)

where CH_{4loss} represents the stratospheric CH_4 sink based on stratospheric CH_4 loss frequencies archived from the NASA Global Modeling Initiative model (Considine et al., 2008; Allen et al., 2010) as described by Murray et al. (2012).

110   The CO simulation in the troposphere is based on Eq. (3):

$$\frac{d[CO_{Trop}]}{dt} = E_{CO} + P(CO) - k_{CO}[OH][CO]$$
(3)

where E_{CO} represents the surface emissions (fossil fuel, biofuel and biomass burning), $P(CO)$ accounts for the chemical production of CO from CH_4 and NMVOC oxidation, $[OH]$ represents the OH concentrations, and k_{CO} is the pressure- and temperature-dependent rate constant for oxidation of CO by OH from the Jet Propulsion Laboratory (JPL) data evaluation
115   (Burkholder et al., 2015). The chemical production of CO ($P(CO)$) can be further separated into the production from CH_4 ($P(CO)_{CH_4}$) and the production from NMVOC ($P(CO)_{NMVOC}$):

$$P(CO) = P(CO)_{CH_4} + P(CO)_{NMVOC}$$
(4)

The $P(CO)_{CH_4}$ and $P(CO)_{NMVOC}$ terms are obtained with the GEOS-Chem full chemistry simulation from the simulated monthly CO chemical production rates ($P(CO)$) as described by Fisher et al. (2017). In brief, the simulated $P(CO)$ is split
120   offline to the $P(CO)_{CH_4}$ and $P(CO)_{NMVOC}$ terms based on the CH_4 loss rates ($L(CH_4)$) that are also simulated and saved from a full chemistry simulation. A 100% CO yield from CH_4 is assumed, hence the production of CO from CH_4 is equal to the CH_4 loss:

$$P(CO)_{CH_4} = L(CH_4)$$
(5)

The remaining $P(CO)_{NMVOC}$ contribution is then calculated as the difference between the total CO production and the production of CO from CH_4:

$$P(CO)_{NMVOC} = P(CO) - P(CO)_{CH_4} \tag{6}$$

Since the 100% yield may overestimate the production of CO from the oxidation of CH_4 the simulation caps the $P(CO)_{CH_4}$ to the total $P(CO)$ where it is greater than $P(CO)$ (Fisher et al., 2017). In the stratosphere Eq. (3) becomes:

$$\frac{d[CO_{Strat}]}{dt} = CO_{prod} - CO_{loss} \tag{7}$$

where CO_{prod} represents the stratospheric production of CO from CH_4, while CO_{loss} is the stratospheric CO sink due to chemical reaction with OH. Both quantities are from the NASA Global Modeling Initiative model.

The stand-alone CO_2 simulation throughout the atmosphere is based on:

$$\frac{d[CO_2]}{dt} = E_{CO_2} + P(CO_2) + D_{CO_2} \tag{8}$$

where E_{CO_2} represents the surface (fossil fuel, biomass burning, biofuel, shipping) and 3-D (aviation) emissions, $P(CO_2)$ accounts for the 3-D chemical production from the oxidation of CO, and D_{CO_2} represents the net source from ocean exchange, balanced and net annual terrestrial exchange. Note that D_{CO_2} can be positive or negative since these processes have negative values in regions where they act as a net sink and positive values where they act as a net source. The chemical source $P(CO_2)$ is a prescribed field that is calculated offline and read in at the start of the simulation. This chemical source is based on the monthly CO loss rates ($L(CO)$) from the GEOS-Chem $4° \times 5°$ full chemistry simulation (Nassar et al., 2010). It is assumed that the CO_2 production is equal to CO loss:

$$P(CO_2) = L(CO) \tag{9}$$

Some of the emission inventories used in the CO_2 simulation already include CO_2 from CO oxidation (effectively assuming prompt oxidation of precursors at the point of emission), but these amounts are only in the form of surface emissions, rather than distributed throughout the atmosphere, leading to a bias in the model (Suntharalingam et al., 2005). With the inclusion of a 3-D chemical source in the CO_2 simulation this bias needs to be corrected by subtracting the CO_2 chemical production "emitted" at the surface (in the emission inventories) from the total CO_2. Nassar et al. (2010) quantified a 0.825 Pg C yr^{-1} global annual value for this surface correction based on emissions of all reactants that undergo oxidation to CO_2 and are included in emission inventories. This includes emissions from fossil fuel, biospheric CH_4 (wetlands, ruminants, rice, termites, landfill) and biospheric NMVOC emissions (isoprene and monoterpene). The emission inventories used for biofuel and biomass burning explicitly accounted for CO_2, CO, CH_4 and NMVOC separately, hence no surface correction was applied.

2.2 Coupled GEOS-Chem simulation

Our updates couple CO_2, CH_4 and CO based on the chemical loss and production between these species.

The starting point of the coupled simulation is the calculation of CH_4 based on Eq. (1) and (2). First, however, we made a minor correction to the treatment of CH_4 loss. In the uncoupled CH_4 simulation, the diurnal variability of OH (based on

155 monthly mean values) was neglected, which would overestimate CH_4 loss at night and underestimate it during the day, with biases of up to 100% in some regions. In other offline GEOS-Chem simulations including CO, OH concentration is scaled to the cosine of the solar zenith angle to approximate diurnal variability. We updated the CH_4 code to also apply the diurnal scaling to the OH field used for CH_4 oxidation in the troposphere. Using a 1-year test simulation for 2005, we found that this change has a negligible impact on global annual tropospheric CH_4 loss. The calculation of the CH_4 loss in the stratosphere is

160 unchanged between the coupled and uncoupled simulations. Due to the negligible difference in the annual CH_4 values with (in the coupled simulation) and without (in the uncoupled simulation) the diurnal cycling we have not run the uncoupled CH_4 simulation with this update for 2006–2017.

In the new coupled simulation, the tropospheric CH_4 loss rates are calculated from the oxidation of tropospheric CH_4 by OH at every time step. As before, a 100% yield of CO from CH_4 oxidation is assumed (Duncan et al., 2007), and the tropospheric

165 CH_4 loss is passed to the CO part of the simulation at every timestep as the chemical production of CO from CH_4 ($P(CO)_{CH_4}$) in the troposphere. The calculation of the CO production in the stratosphere and from NMVOCs uses the same method as in the uncoupled CO-only simulation. In the troposphere, the total chemical production of CO ($P(CO)$) is equal to the sum of the archived $P(CO)_{NMVOC}$ field and the now online calculated $P(CO)_{CH_4}$.

The chemical production of CO_2 ($P(CO_2)$) is then calculated from the simulated CO loss from the oxidation of CO by OH

170 in the troposphere and from archived CO loss in the stratosphere. As in the uncoupled version, a 100% yield of CO_2 from CO is assumed (Nassar et al., 2010). For the chemical surface correction, due to the inclusion of the chemically produced CO_2 in other emission inventories, we retain the same correction method and values as in the uncoupled simulation (Nassar et al., 2010).

The new coupling now allows time-specific changes and tracking of the chemical production terms. This is an improvement

175 to the uncoupled simulations where the prescribed fields were based on simulations of specific prior years, and therefore could not capture the year-specific variations and dependencies between these gases. In the uncoupled CO_2, CH_4 and CO simulations, all the prescribed chemical production and loss fields were monthly mean values, while with the coupled simulation these fields are now calculated online at every timestep (i.e., 20 min), allowing us to track the day-to-day and diurnal variability of the simulated chemical production terms. A schematic diagram of the coupling is shown in Fig. 1.

180 **2.3 OH fields**

The OH fields have a significant impact on the chemical production and loss terms. The uncoupled carbon gas simulations in the default v12 GEOS-Chem model all use OH fields saved from different versions of the full chemistry model: GEOS-Chem v5-07-08 for the CH_4 simulation (Park et al.), v9-01-03 for the CO simulation (Fisher et al., 2017), and v8-02-01 for the CO_2 simulation (Nassar et al., 2010).

185 In our coupled simulation, the more recent v9-01-03 OH fields are used for all aspects of the simulation. However, the loss calculations do not feed back to OH and this aspect remains uncoupled. To test the impact of the different OH fields on the
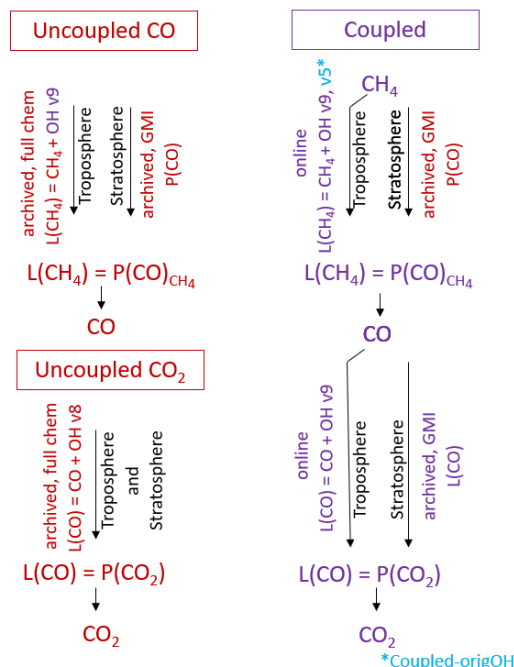
Figure 1. Schematic diagram of the uncoupled CO and CO_2 simulations (left) versus the coupled CH_4–CO–CO_2 simulation (right). The diagram also shows the OH field versions used between simulations, as described in the text (uncoupled CO: v9-01-03, uncoupled CO_2: v8-02-01, coupled: v9-01-03, *coupled-origOH*: v5-07-08 (CH_4 loss) and v9-01-03 (CO loss)). Colors correspond to simulations shown in subsequent sections (see text for details). Note, both simulations use the same $P(CO)_{NMVOC}$ field described in Sect. 2.1 (not shown on diagram).

chemical production and loss terms, we performed a sensitivity test where we retained the default version of the OH used in the CH_4 uncoupled simulation (i.e., v5-07-08 OH for the calculation of $L(CH_4)$). We will refer to this as the *coupled-origOH* simulation. A summary of the OH field versions is shown in Fig. 1.

190   The global annual mean OH is largest in the v8-02-01 full chemistry simulation (11.8×10^5 molecules cm^{-3}) followed by v9-01-03 (11.4×10^5 molecules cm^{-3}) and v5-07-08 (10.8×10^5 molecules cm^{-3}) (http://wiki.seas.harvard.edu/geos-chem/index.php/Mean_OH_concentration). Figure 2 shows the yearly change of the OH fields used in the simulations. At the surface, v9-01-03 OH shows a peak during Northern Hemisphere (NH) summer (July), while v8-02-01 and v5-07-08 have an earlier peak in June; however, v5-07-08 also shows a second peak in October when the other two OH fields suggest a decline (Fig. 2).

195   The seasonal cycles at higher altitudes are more consistent between simulations.

Figure 3 shows the annual global spatial patterns of the OH fields. At the surface, the v9-01-03 OH fields are globally higher than v5-07-08 and lower than v8-02-01. Relative to v9-01-03, v5-07-08 shows lower surface OH above most land regions and NH ocean regions, while v8-02-01 only shows lower surface OH in tropical land regions and NH mid-latitude ocean regions, with higher OH elsewhere (Fig. 3). A similar pattern is observed at higher altitudes (500 hPa), with smaller and more
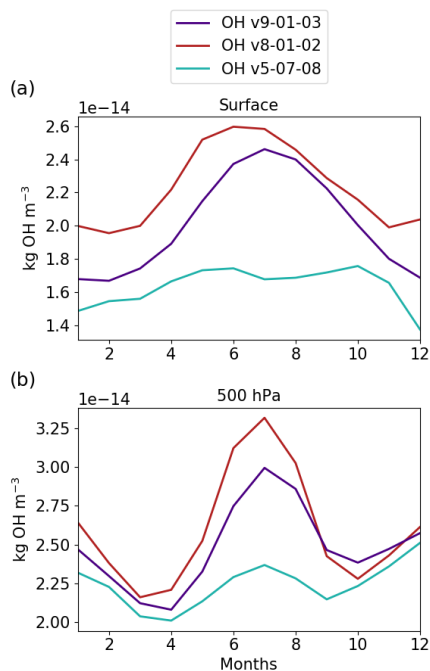
Figure 2. Globally averaged OH fields at the surface (a) and at 500 hPa (b) from the v9-01-03 (indigo, used by uncoupled CO and coupled simulation), v8-02-01 (red, uncoupled CO_2) and v5-07-08 (turquoise, uncoupled CH_4 and *coupled-origOH*) full chemistry simulations.

200   diffuse differences. The seasonal plots of the global surface distributions can be found in the Supplement, Fig. S2. Overall, we find significant differences between the OH fields used in the individual uncoupled simulations. These differences can have a large impact on the production and loss terms, as well the resulting mole fractions, which we test in what follows using the *coupled-origOH* sensitivity simulation. Going forward, we recommend that common OH fields should also be adopted for all uncoupled simulations in GEOS-Chem.

205 **3   Chemical production and loss budgets**

The main terms impacted by the coupling of CH_4, CO and CO_2 are the production of CO from CH_4 ($P(CO)_{CH_4}$) in the troposphere and the production of CO_2 from CO ($P(CO_2)$). Furthermore, the changes in these terms also impact the total source budgets for CO and CO_2 and the sink term for CO (loss of CO by OH ($L(CO)$)). Note, the tropospheric CH_4 loss by OH ($L(CH_{4Trop})$) is also different in the coupled simulation due to the inclusion of a diurnal OH cycle; however, as discussed
210   in Sect. 2.2 the impact of this update is negligible on the annual scale, and, as it is not a direct result of the coupling it is not further discussed here.
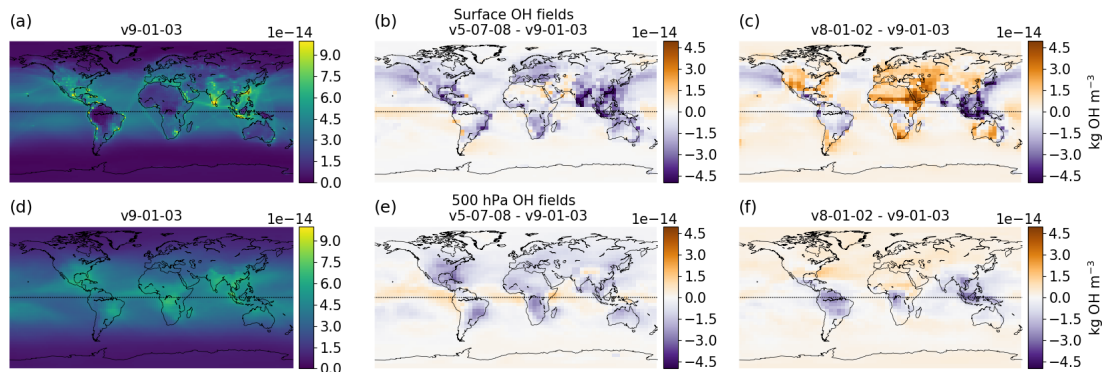
Figure 3. Surface (a–c) and 500 hPa (d–f) yearly averaged global spatial distribution of the OH fields based on the v9-01-03 (a, d) full chemistry simulation and the difference between v5-07-08 - v9-01-03 (b, e) and v8-02-01 - v9-01-03 (c, f).

We separate the analysis of our results into two parts: i) the impact of the coupling evaluated by comparing the uncoupled and coupled simulations and ii) the impact of using different OH (hereinafter referred to as the OH disconnect) evaluated by comparing the coupled simulation with the *coupled-origOH*.

3.1 Impact of the coupling

The annual global budgets of $P(CO)_{CH_4}$ and $P(CO_2)$ from the uncoupled and coupled simulations are shown in Fig. 4. The regional distribution of the annual production budgets, results from the *coupled-origOH* simulation and additional loss terms can be found in Fig. S3–S6.

We find an increase in $P(CO)_{CH_4}$ with time over the 2006–2017 period in the coupled simulation (Fig. 4b) due to increasing CH_4 mixing ratios, and hence increased CH_4 loss that is the most pronounced in tropical regions (Fig. S3). The $P(CO)_{CH_4}$ field in the uncoupled simulation (Fig. 4a) is based on 2009–2011 average values and therefore does not allow simulation of year-to-year changes. Different El Niño Southern Oscillation-triggered CH_4 processes lead to opposite changes in CH_4: during El Niño events, wetland emissions are reduced, while biomass burning emissions are enhanced (Dlugokencky et al., 2011; Hodson et al., 2011; Schaefer et al., 2018; Rowlinson et al., 2019). Our coupled simulation shows that these changes have important implications for the chemical production of CO that are not captured in the uncoupled simulation. We observe the strongest growth in the $P(CO)_{CH_4}$ during 2015/16, which coincidences with one of the strongest El Niño years, while we find no growth during 2010/11, a strong La Niña year, highlighting the impact of climate anomalies on the chemical terms. The availability of OH via CO also impacts the CH_4 interannual variability; however, we are unable to quantify the OH-driven changes here as none of our simulations include OH interannual variability or OH-feedbacks. We recommend future updates to the coupled simulation such as the prioritised inclusion of a CO–OH–CH_4 feedback in the calculation (Holmes, 2018).

Figure 5 shows the change of the budgets throughout the year for each chemical term in different latitudinal bands. Figure 5a shows that both the uncoupled (red) and coupled (indigo) $P(CO)_{CH_4}$ have a similar annual cycle, with overall stronger

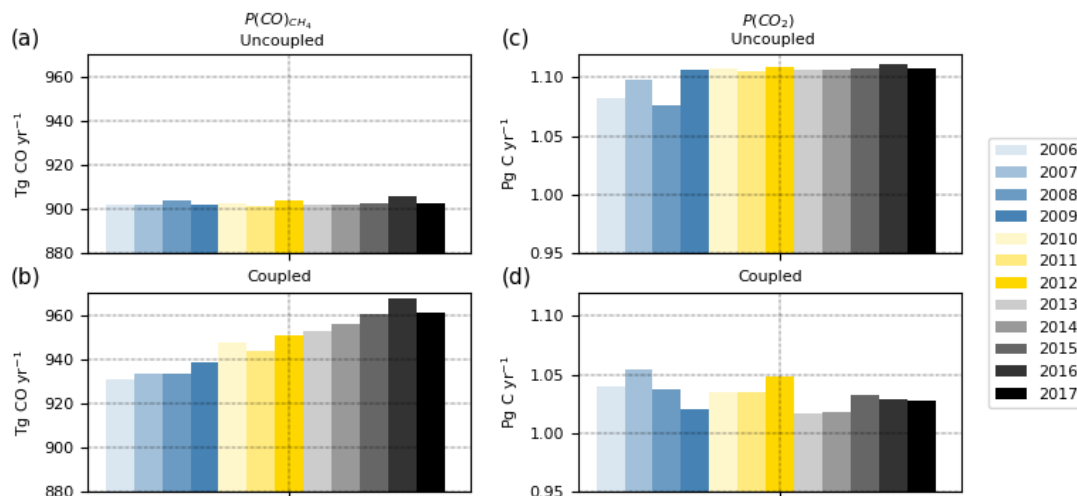**Figure 4.** Annual values of the global chemical term budgets for CO production from CH_4 (a, b) and CO_2 production from CO (c, d) from the uncoupled (a, c) and coupled (b, d) simulations.
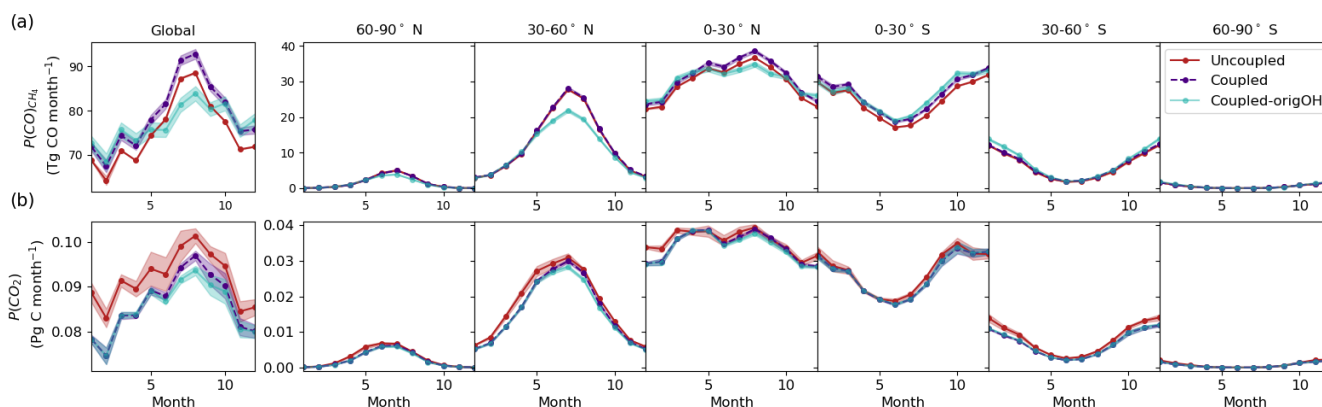

Figure 5. Monthly changes of the CO production from CH_4 (a) and CO_2 production from CO (b), with 1 standard deviation, from the uncoupled (red), coupled (indigo) and *coupled-origOH* (turquoise) simulation (averaged for 2006–2017).

production in the coupled simulation. The coupled simulation also shows stronger variability due to the year-specific CH_4 loss, with the strongest variability in tropical regions.

235   The $P(CO_2)$ in the uncoupled simulation has year-specific fields only for 2004–2009 (Nassar et al., 2010) (Fig. 4c); hence in contrast to the coupled simulation (Fig. 4d) it is missing information about the temporal change of this term after 2009. Although covering a shorter time period, from 2006 to 2009, the $P(CO_2)$ in the uncoupled simulation shows stronger vari-

11

Geoscientific
Model Development
Discussions
EGU
Open Access

Table 2. Global and regional budgets for CH_4 loss in the troposphere ($L(CH_{4Trop})$ in Tg CH_4 yr^{-1}), CO production from CH_4 ($P(CO)_{CH_4}$ in Tg CO yr^{-1}), CO loss from OH ($L(CO)$ in Tg CO yr^{-1}) and CO_2 production from CO ($P(CO_2)$ in Pg C yr^{-1}) from the uncoupled (U) and coupled (C) simulations, as well literature values for the global budgets. The budgets from the simulations are shown as a multi-year mean based on years 2006–2017. The range of values for individual years is shown in the parentheses.

Chemical terms	Prior Work	Global U	Global C	NH U	NH C	SH U	SH C
$L(CH_{4Trop})$	$382–617^{a,b,c}$	476^d	510 (501–522)	263^d	294 (289–301)	213^d	216 (212–220)
$P(CO)_{CH_4}$	$760–1086^{e,f,g,h,i}$	902^j $(901–905)^j$	947 (931–967)	521^j $(520–522)^j$	542 (532–553)	381^j $(380–382)^j$	405 (398–413)
$L(CO)$	$2478–2630^{f,k,l,m}$	2363^j $(2320–2426)^j$	2408 (2370–2457)	1438^j $(1417–1466)^j$	1461 (1446–1479)	924^j $(900–962)^j$	946 (923–978)
$P(CO_2)$	$1.04–1.1^{n,o}$	1.1^p $(1.08–1.11)^p$	1.03 (1.02–1.05)	0.67^p $(0.63–0.68)^p$	0.63 (0.62–0.63)	0.43^p $(0.43–0.46)^p$	0.41 (0.40–0.42)

[a] Wuebbles and Hayhoe (2002), base year: only the "best guess" estimates are shown, based on a range of values, [b] Ciais et al. (2014), base year: 1980–1989, [c] Wang et al. (2004), base year: 1994, [d] Based on 2005 only, the 2005 values in the coupled simulation are Global: 501 Tg CH_4 yr^{-1}, NH: 289 Tg CH_4 yr^{-1}, SH: 211 Tg CH_4 yr^{-1}, [e] Holloway et al. (2000), base year: not defined, [f] Bergamaschi et al. (2000), base year: 1993–1995, [g] Duncan et al. (2007), base year: 1988–1997, [h] Arellano Jr. and Hess (2006), base year: 2000–2001, [i] Zeng et al. (2015), base year: 2004, range based on different model simulations. [j] Fisher et al. (2017), base year: 2009–2011 average, [k] Pétron et al. (2004), [l] Arellano Jr. and Hess (2006), [m] Nassar et al. (2010), base year: 2004–2010, these are the fields used in the uncoupled CO_2 simulation, 100% yield from $L(CO)$ loss to $P(CO_2)$, NH:1446–1558 Tg CO yr^{-1}, SH:1003–1075 Tg CO yr^{-1}, [n] Nassar et al. (2010), base year: 2000–2009, [o] Suntharalingam et al. (2005), base year: 1988–1997, [p] Nassar et al. (2010), base year: 2006–2009.

ability relative to the coupled one (Fig. 5b). The uncoupled simulation also shows stronger $P(CO_2)$ values in all latitudinal bands; however, the largest difference between simulations is during December–March mostly in NH tropical and Southern

240 Hemisphere (SH) mid-latitude regions. The stronger uncoupled $P(CO_2)$ values are a result of different CO amounts used for the CO loss calculation between the coupled and full chemistry simulations in GEOS-Chem, as well as more abundant OH used to calculate $L(CO)$ for the uncoupled simulation (v8-02-01, Fig. 2) relative to the OH field used in the coupled simulation (v9-01-03), discussed in Sect. 2.3.

The global and regional budgets for the chemical components for both coupled and uncoupled versions of the model along
245 with known literature values are shown in Table 2. The results from our coupled simulation are in good agreement with values from prior work. In summary, the coupled simulation shows stronger $P(CO)_{CH_4}$ than the uncoupled simulation due to the stronger CH_4 loss for all years and for both hemispheres (29–61 Tg CO yr^{-1} difference). This difference represents 1.2–2.6% of the total CO source in the coupled simulation. The CO_2 chemical source shows weaker values in the coupled simulation relative to the uncoupled one (0.04–0.09 Pg C yr^{-1} difference). This difference represents 0.3–0.7% of the total CO_2 source
250 in the coupled simulation.

3.2 Impact of the OH disconnect

As described in Sect. 2.3, we perform a sensitivity simulation (*coupled-origOH*) with the coupled simulation but using the default OH field from the uncoupled CH_4 simulation when calculating the chemical loss terms in order to highlight the impact of inconsistent OH fields on the simulated values. Using the default v5-07-08 OH fields for the $L(CH_{4Trop})$ calculation results

255   in a 9–22 Tg CH_4 yr^{-1} global decrease relative to the coupled simulation (Fig. S3), with weaker CH_4 loss in the *coupled-origOH* simulation due to the lower OH (Fig. 2). Relative to the standard coupled simulation, the *coupled-origOH* sensitivity simulation shows weaker CH_4 loss globally and in the NH, and stronger loss in the SH due to higher OH values over the SH ocean regions (Fig. S3 and Fig. 3).

Figure 5a shows that the weaker CH_4 loss in *coupled-origOH* also results in weaker global CO production from CH_4

260   (16–39 Tg CO yr^{-1} difference). As with the $L(CH_{4Trop})$, the stronger coupled simulation values are only present in the NH, while in the SH the *coupled-origOH* results show stronger $P(CO)_{CH_4}$. As in the coupled simulation, the *coupled-origOH* simulation shows an increase in the $P(CO)_{CH_4}$ with time due to the increased CH_4 loss. Relative to the coupled results, the *coupled-origOH* $P(CO)_{CH_4}$ (Fig. 5a, turquoise line) globally shows stronger production between September–May and weaker production between June–August, with the largest difference in mid-latitude regions in the NH. These differences are

265   exclusively driven by differences in the OH fields.

In contrast to the $P(CO)_{CH_4}$ values, using the v5-07-08 OH fields for the $L(CH_{4Trop})$ calculation has a negligible impact on $P(CO_2)$. This is expected since the $L(CH_{4Trop})$ has only an indirect and minor contribution when calculating $P(CO_2)$. Both the *coupled-origOH* and coupled simulations show similar $P(CO_2)$ budgets but with stronger production in the coupled simulation between July–October (Fig. 5b).

270   4   Chemical source contributions

Due to the linearity of the GEOS-Chem carbon greenhouse gas simulations, in addition to simulating the total amount of each gas, we can also quantify the mole fractions of individual processes (referred to as tracers). These include the CO_2 mole fraction from CO_2 chemical production (CO_{2CO}) and the CO mole fraction from CO production from CH_4 (CO_{CH_4}). Figure 6 shows these chemical production tracers (Fig. 6a, b), as well the total CO and CO_2 mole fractions (Fig. 6c, d) at the surface

275   for different latitudinal bands. Note, in contrast to the CO source tracers where the atmospheric sink terms (e.g., OH) are applied to each tracer, for CO_2 there is no sink applied to the different source tracers. This leads to a trend in CO_{2CO} and its accumulation in the atmosphere. To highlight differences in the seasonal cycle we have detrended the CO_{2CO} data shown in Fig. 6b, d and added the mean 2006–2017 yearly growth rates.

Implementing the online calculation of the chemical terms results in higher CO_{CH_4} values in the coupled simulation relative

280   to the uncoupled along with stronger variability (Fig. 6a), similar to the production rates (Table 2, Fig. 5a). An average 1.2 ± 0.5 ppb difference is present across the NH between the coupled and uncoupled results while in the SH we find a larger difference of 1.8 ± 0.5 ppb. Both the coupled and uncoupled simulations show similar seasonal cycles; however, using inconsistent OH fields between simulations led to significant differences in the CO_{CH_4} seasonal cycles. In the *coupled-origOH* simulation,
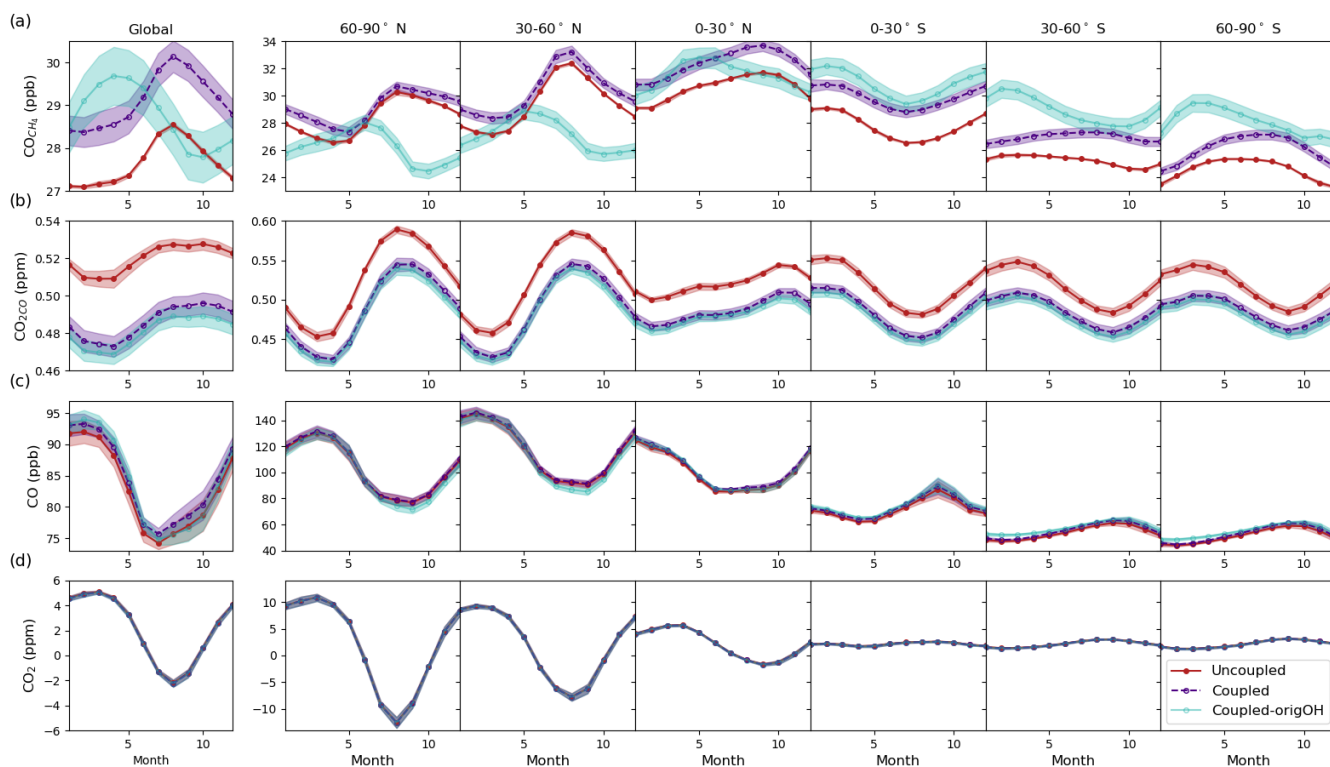
Figure 6. Surface mole fractions from chemical production of CO_{CH_4} (a) and CO_{2CO} (b) and total CO (c) and CO_2 (d) mole fractions from the uncoupled (red), coupled (indigo) and *coupled-origOH* (turquoise) simulations with 1 standard deviation (based on 2006–2017 average values). Note, the CO_2 values are detrended and added to the mean 2006–2017 yearly growth rates.

the mole fractions have a reversed seasonal cycle relative to both the coupled and uncoupled results, with the reversal most
pronounced in the NH mid-latitude and polar regions. A 2.3 ± 2 ppb difference is present in the NH between the coupled and
coupled-origOH results, with higher values in the coupled simulation, while in the SH we find a -1.7 ± 1.1 ppb difference, with
higher values in the *coupled-origOH* simulation. The difference in the seasonal cycles is also reflected in the total amounts of
CO (Fig. 6c); however, globally the total CO has the same seasonal cycle in all three simulations, since the contribution of
CH_4 oxidation is only ≈ 35 % of the total CO.

To understand the origin of the differences in the seasonal cycles we add an additional chemical term to the analysis,
$L(CO_{CH_4})$ that represents the loss of CO_{CH_4} via OH, which is a sub-component of the total $L(CO)$. The difference between
the production ($P(CO)_{CH_4}$) and loss ($L(CO_{CH_4})$) together with transport leads to the modelled CO_{CH_4} mole fractions. Figure
7 shows the global surface and 500 hPa altitude $P(CO)_{CH_4}$, $L(CO_{CH_4})$ and their difference from the uncoupled, coupled and
coupled-origOH simulations and Fig. S7 shows the change of these terms in the NH versus SH. Both at the surface and in the
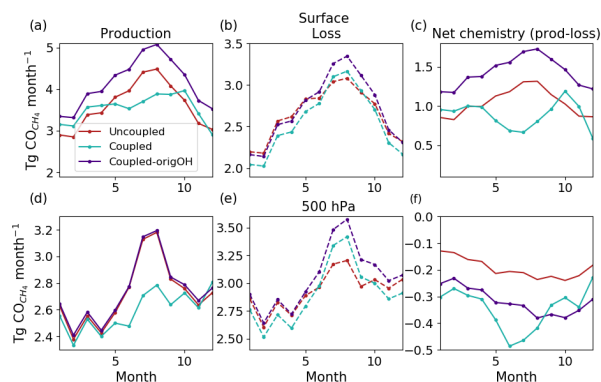
14

Figure 7. Global production of CO from CH_4 (a, d), its loss via OH (b, e) and their difference (c, f) in the uncoupled (red), coupled (indigo) and *coupled-origOH* (turquoise) simulations at the surface (a–c) and 500 hPa altitude (d–f), averaged for 2006–2017.

tropospheric column, the *coupled-origOH* simulation results show low production in June–August, a period when we observe the maximum production in both the uncoupled and coupled simulation, leading to an opposite seasonal cycle. As already discussed, $P(CO)_{CH_4}$ in the troposphere is calculated based on a 100% yield from the CH_4 loss via OH, hence the $P(CO)_{CH_4}$ and resulting CO_{CH_4} mole fraction differences are a result of the differences in the $L(CH_{4Trop})$ fields. The main difference in the CH_4 loss calculation between the *coupled-origOH* versus the uncoupled and coupled simulation is the version of the OH field. The v5-07-08 OH field used in the *coupled-origOH* simulation results in weaker $L(CH_{4Trop})$ during NH summer, which leads to weaker $P(CO)_{CH_4}$ and significant differences in the net chemistry (production-loss) and resulting mole fractions. We find that this difference is the most pronounced at the surface while at higher altitudes it slowly diminishes. Although further differences exist in the $L(CH_{4Trop})$ calculation between simulations, we find that the choice of the OH field is the dominant driver of the resulting discrepancies. The additional differences are described in the Supplement, Sect. S1.

The CO_{2CO} mole fractions show a similar seasonal cycle between all three simulations in both hemispheres with a stronger seasonal cycle in the uncoupled simulation (i.e., stronger amplitude) in all regions except the NH tropics (Fig. 6b). The uncoupled simulation due to the stronger chemical production shows a stronger yearly global surface growth rate of 0.52 ppm yr^{-1}, followed by the coupled simulation, 0.49 ppm yr^{-1}, while the *coupled-origOH* shows a weaker growth rate of 0.48 ppm yr^{-1} due to weaker production. Overall, both the coupling and OH disconnect do not significantly impact the resulting mole fractions between simulations. Moreover, the differences between the coupled and uncoupled simulations are too small to be reflected in the total CO_2 surface values (Fig. 6d). As already highlighted $P(CO_2)$ is a 3-D source, hence the signal of this source in the surface mole fractions is small relative to the other more dominant CO_2 surface fluxes.

5 Global distribution

Figure 8 shows the total column chemical production of CO from CH_4 with corresponding mole fractions at the surface and 500 hPa altitude from the three simulations, as well as their differences. $P(CO)_{CH_4}$ and $L(CH_4)$ have the same spatial

and temporal distribution due to the 100 % yield. Figure 9 is the same as Fig. 8 but for the chemical production of CO_2. Similarly, both $P(CO_2)$ and $L(CO)$ have the same spatial and temporal distribution due to the 100 % yield. For CO_2 we have additionally removed the long-term trend from the CO_{2CO} mole fractions, as discussed in Sect. 4. The seasonal changes of both the productions and mole fractions are shown in Fig. S8–S11 for CO and Fig. S12–S15 for CO_2.

320   5.1   Impact of the coupling

The online calculation of $P(CO)_{CH_4}$ has a small impact on its global spatial distribution - both the coupled and uncoupled simulations show similar results (Fig 8a, b). The simulations use the same OH fields, hence the differences in the $P(CO)_{CH_4}$ are driven by different handling of the CH_4 values before the OH loss is applied (Supplement Sect. S1). The main difference between the two simulations is the stronger $P(CO)_{CH_4}$ over tropical ocean regions and weaker $P(CO)_{CH_4}$ over NH land

325   regions in the coupled version. $P(CO)_{CH_4}$ shows a seasonal cycle with maximum production during NH summer and minimum during winter, the opposite of the seasonal cycle of the total CO mole fractions (Fig. S12–S15). On a yearly scale, the surface CO_{CH_4} mole fractions from the coupled simulation show higher values above both ocean and land regions (Fig 8i), as a result of the stronger $P(CO)_{CH_4}$ over tropical ocean regions. A similar behavior is observed at 500 hPa; however, the differences are smaller and more diffuse. We observe the same differences throughout the seasons. The seasonal change of the resulting mole

330   fractions depends on the change of the production and loss ratio (Sect. 4), as well the impact of transport, and can differ from the seasonal cycle of the production fields. We further discuss the simulated mole fractions and the impact of the coupling on total CO in Sect. 6.

The coupled simulation shows stronger $P(CO_2)$ (Fig 9b) in certain land regions, despite the annual global chemical source being weaker than in the uncoupled simulation by 0.04–0.1 Pg C yr^{-1}. South America, Central Africa, Indonesia, parts of East

335   Asia and Australia show stronger CO_2 chemical production relative to the uncoupled simulation. Moreover, in the uncoupled simulation there is almost no $P(CO_2)$ observed above the Amazon (Nassar et al., 2010); however, our results suggest the opposite. The difference patterns appear to be mostly independent of season (Fig. S12–S15). The chemical production is overall stronger above the ocean in the uncoupled simulation for all seasons; however, the coupled simulation does show stronger $P(CO_2)$ during certain periods in tropical and NH mid-latitude regions. The stronger $P(CO_2)$ above South America, Central

340   Africa, Indonesia, parts of East Asia and Australia shown in the yearly average fields are present in all seasons; but with the strongest contribution during September–November. South America, Central Africa and northern Australia are characterized by strong biomass burning, especially during the SH dry season when frequent fires are observed (September–November), emitting large amounts of CO into the atmosphere (Edwards et al., 2006). Our coupled model simulates the $P(CO_2)$ in these regions during the fire season to be stronger than the previous fields used in the uncoupled simulation. The stronger

345   $P(CO_2)$ from the coupled simulation in other regions such as East Asia and North America point to enhanced anthropogenic CO emissions that lead to stronger chemical production of CO_2. In addition to the primary CO emissions, the secondary production of CO from NMVOC could also have a significant impact on the $P(CO_2)$ in regions where we observe differences. Different model versions were used to save the $P(NMVOC)$ and $P(CO_2)$. The updated chemistry between model versions
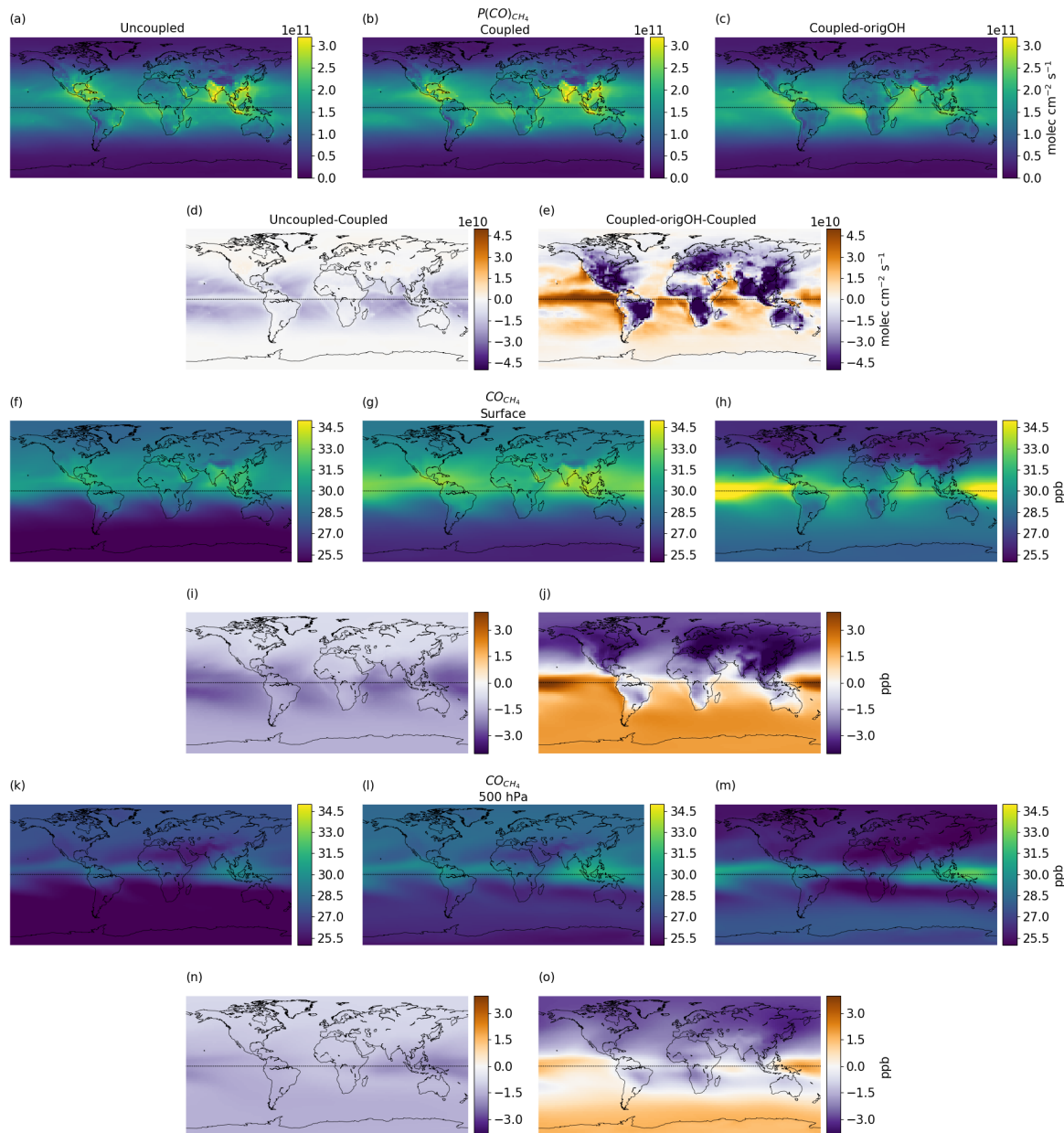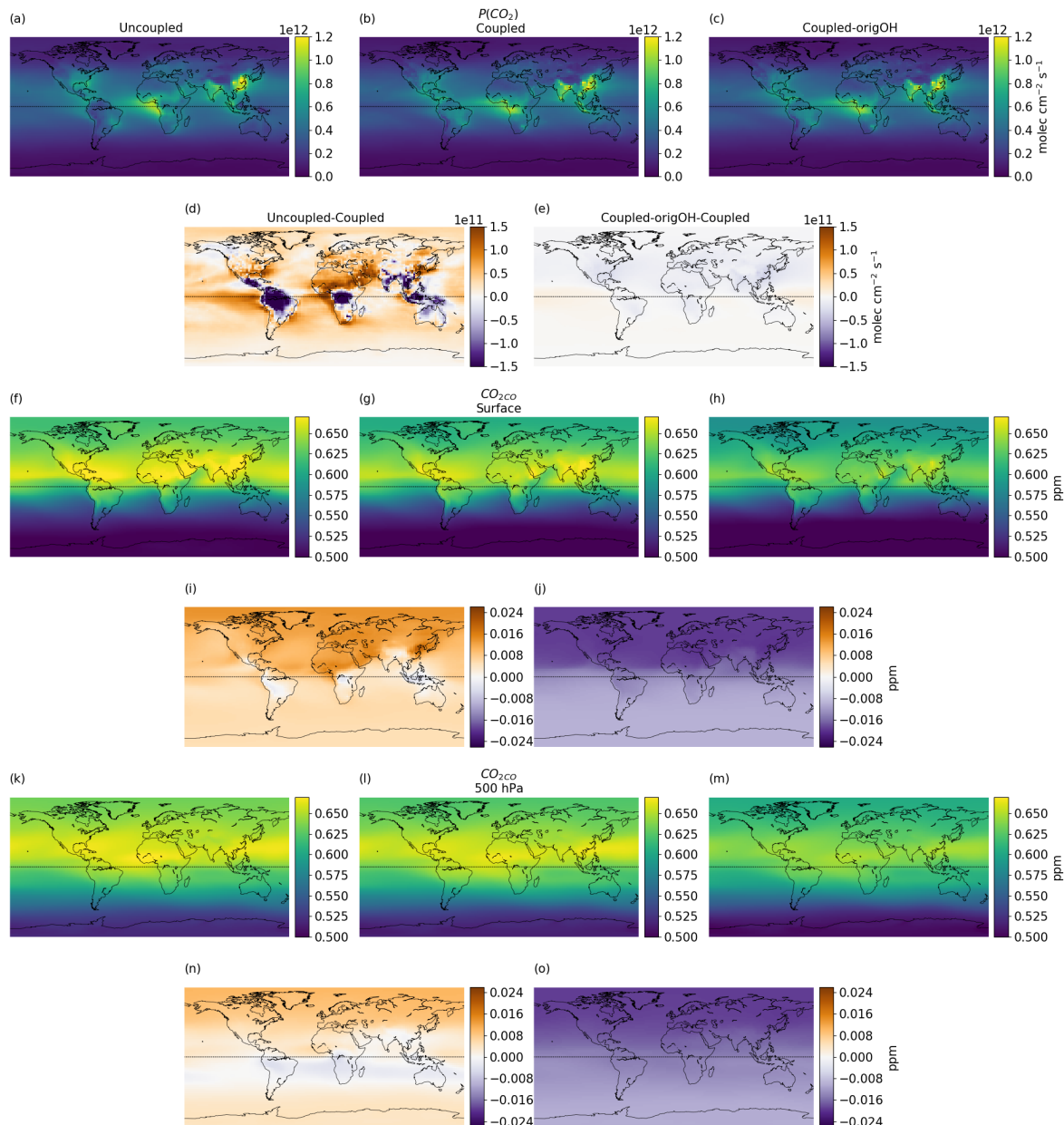
Figure 8. Average 2006–2017 total column CO chemical production from CH_4 (a–e), corresponding mole fractions (i.e., CO_{CH_4}) at the surface (f–j) and at 500 hPa (k–o) based on the uncoupled (a, f, k), coupled (b, g, l) and *coupled-origOH* (c, h, m) simulations, and their difference relative to the coupled simulation (d, e, i, j, n, o).

would additionally impact the $P(CO_2)$ through the CO production from NMVOC in regions where we expect a significant
350   contribution from this production term (e.g., the Amazon).

17

Figure 9. Average 2006–2017 total column CO_2 chemical production from CO (a–e), corresponding mole fractions (i.e., CO_{2CO}) at the surface (f–j) and at 500 hPa (k–o) based on the uncoupled (a, f, k), coupled (b, g, l) and *coupled-origOH* (c, h, m) simulations, and their difference relative to the coupled simulation (d, e, i, j, n, o).

The spatial distribution of the mole fractions is similar between simulations with overall higher values in the uncoupled simulation due to the globally stronger $P(CO_2)$, with higher mole fractions in the NH. However, the coupled simulation does

show more abundant CO_{2CO} over land regions with stronger $P(CO_2)$, with larger differences at higher altitudes. The full chemistry simulation that was used to create the uncoupled simulation $P(CO_2)$ fields was run on lower resolution ($4°x5°$),

355   hence the uncoupled $P(CO_2)$ field is more diffuse relative to the coupled simulations.

5.2   Impact of the OH disconnect

Although we do not find significant differences in the $P(CO)_{CH_4}$ global spatial distribution between the coupled and uncoupled simulation, the *coupled-origOH* results show significant differences (Fig. 8c). We find stronger production over the ocean and weaker production above land regions in the *coupled-origOH* simulation relative to both the coupled and uncoupled

360   simulations. The $P(CO)_{CH_4}$ in the coupled simulation shows stronger values than in the *coupled-origOH* during all seasons, with the largest difference during summer periods for each hemisphere and larger differences in the NH; however, the difference over the ocean has a weaker seasonality. The CO_{CH_4} mole fractions at the surface are highest in the tropical ocean regions in the *coupled-origOH* simulation due to the stronger chemical production in these regions. The *coupled-origOH* simulation also shows lower mole fractions in the NH and higher values in the SH; however, with lower mole fractions in parts of the SH,

365   Africa and South America. Due to a coarser resolution of the OH fields in the *coupled-origOH* ($4°x5°$) relative to the OH fields in the uncoupled and coupled simulations ($2°x2.5°$), the $L(CH_4)$ and $P(CO)_{CH_4}$ field in the *coupled-origOH* simulation is also more diffuse.

The same OH field is used to calculate the $L(CO)$ and $P(CO_2)$ in the coupled and *coupled-origOH* simulation (Fig 9b, c), hence the $P(CO_2)$ is only impacted by differences in $P(CO)_{CH_4}$ through $L(CH_4)$ that relies on different OH fields. Both

370   simulations show similar spatial distribution, with stronger $P(CO_2)$ in the coupled simulation over land regions and in the NH. Differences in the mole fractions are also minimal; however, with higher values in the coupled simulation, especially in the NH.

5.3   Vertical latitudinal distribution

Figure 10 shows the vertical latitudinal distribution of $P(CO)_{CH_4}$ and $P(CO_2)$ for different months, averaged for 2006–2017,

375   as well as the differences between simulations relative to the coupled simulation.

The strongest $P(CO)_{CH_4}$ in the coupled simulation occurs between the surface and 3 km altitude. For most months, this chemical production is stronger in the NH relative to the SH; however, around November we observe a stronger production in the SH, potentially due to biomass burning and wetland activity that leads to higher CH_4 levels and subsequent loss. Although the strongest production occurs between $50°$ S–$50°$ N, we also observe production in SH polar regions in November–January

380   and in Arctic regions in May–July, corresponding to their summer periods. The Arctic regions shows stronger production relative to the Antarctic regions, due to higher CH_4 levels and stronger loss in the NH. As for the global spatial distribution results, the coupling has a small impact on the vertical distribution (Figure 10b, stronger production in the coupled) while the OH disconnect shows larger differences (Figure 10c). The largest difference between the coupled and *coupled-origOH* simulation occurs in July–September, when the coupled simulation suggests stronger production at the surface in SH mid-

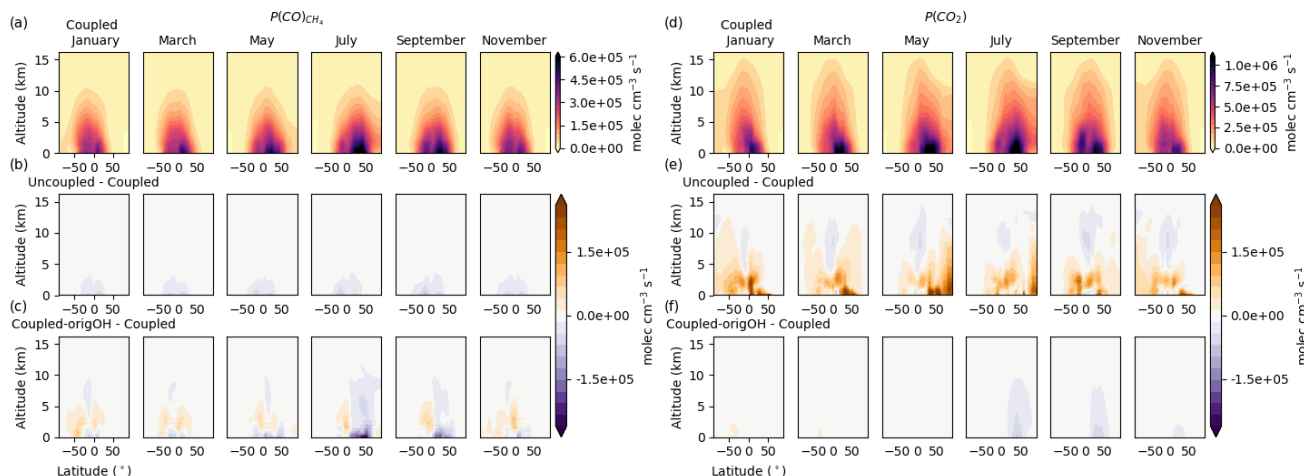385   latitude regions and weaker production in the NH.

19

Figure 10. Vertical latitudinal distribution of the coupled CO chemical production from CH_4 (a) and CO_2 chemical production from CO (d) and the uncoupled (b, e) and *coupled-origOH* (c, f) differences relative to the coupled simulation, for different months, averaged for 2006–2017.

The strongest CO_2 chemical production in the coupled simulation occurs between the surface and 4 km altitude and CO_2 is produced chemically up to 15 km (Figure 10d). Between January–July we observe stronger production in the NH, with the strongest production in tropical regions at the beginning of the year, moving towards higher latitudes by July. Based on the distribution (Fig. 9) of this source in the NH, strong production occurs over China and India from anthropogenic 390   CO, with mixed biomass burning from other regions. For the remaining months, both hemispheres show strong $P(CO_2)$, with the SH showing stronger production in September, presumably due to additional biomass burning in the tropics (e.g., Indonesia, Australia, Africa, S America). Nassar et al. (2010), based on results from the uncoupled simulation, did not find a biomass burning contribution over the Amazon; however, our coupled simulation, as already discussed, suggests a significant contribution from this region. Relative to the uncoupled simulation, the coupled simulation shows weaker production in mid-395   latitude and polar regions, with stronger contribution in the tropics at surface levels and above 5 km. The Arctic and Antarctic regions show weaker production in the coupled simulation. As for the global spatial distribution, the $P(CO_2)$ values between the coupled and *coupled-origOH* simulations are similar; however, with stronger production in the coupled.

6   Simulation comparison with measurements

We validate the new coupled simulation against global column retrievals, calibrated surface flask and aircraft in situ mea-400   surements (Fig. 11, Table A1). Long-term time series of column averaged dry air mole fraction measurements of CO_2, CH_4 and CO are measured by TCCON (Wunch et al., 2011). In addition, long-term time series of surface mole fractions exist at different sites across the globe as part of NOAA GGGRN (Dlugokencky et al. (2020b, a); Petron et al. (2020)). For vertical
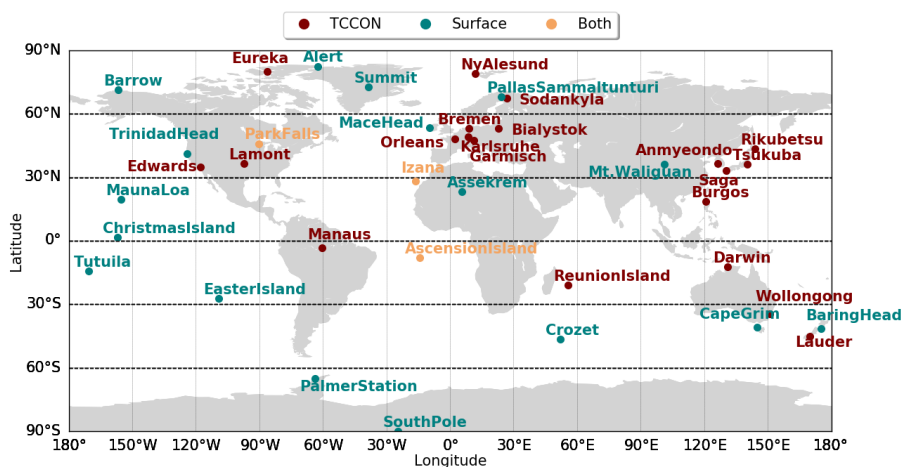
Geoscientific
Model Development
Discussions

Figure 11. Locations of the flask surface sites from NOAA GGGRN (turquoise, Dlugokencky et al. (2020b, a); Petron et al. (2020)) along with sites that measure column-averaged dry air mole fractions as part of TCCON (red, https://tccondata.org/) and sites that are both part of TCCON and NOAA GGGRN (orange). For site details, see Table A1.

profile comparison we use aircraft measurements from the ATom campaigns (Wofsy et al., 2018). For CO_2 and CO we use the merged ATom data product collected from the NOAA-Picarro and Harvard Quantum Cascade Laser System instrument while

405 for CH_4 we use the measurements collected with the NOAA-Picarro instrument only.

We use column measurements from TCCON as the main data product to highlight the differences between the uncoupled and coupled simulations. Both the CO and CO_2 chemical sources are produced throughout the column, hence relative to surface measurements these measurements are more representative of the impact of chemical production on the total amounts of the gases. To compare the total CO and CO_2 model output with the column averaged measurements, we convert the modelled

410 mole fractions to column averaged dry-air mole fractions (X_{gas}) by dividing the vertical column of the gas of interest (Ω_{gas}) with the total dry air column (Ω_{O_2}), based on the method described by Wunch et al. (2010):

$$X_{gas} = 0.2095 \frac{\Omega_{gas}}{\Omega_{O_2}} \tag{10}$$

and smoothed according to Eq. (11) (Deutscher et al., 2014):

$$c_s = c_a + h^T a^T (x_m - x_a) \tag{11}$$

415 where c_s represents the smoothed column model dry-air mole fraction, c_a is the TCCON a priori column dry-air mole fraction, h^T represents the vertical column summation, a^T is the the Fourier-Transform Spectrometer averaging kernel, and x_m and x_a are the model and a priori dry-air mole fraction profiles.

The modelled vertical profiles are saved at a daily temporal resolution and extracted for the closest grid box to each TCCON station. For the comparison with surface measurements, we extract the grid points at the lowest level in the model. For comparison with aircraft measurements, model outputs are saved for grid boxes corresponding to the measured time, latitude, longitude and level along the plane flight track. Both the aircraft measurements and modelled output are averaged to the model temporal (20 min) and spatial ($2°$x$2.5°$) resolution to calculate one average value for each unique grid-box-time-step combination.

The 10 year spinup that is performed prior to the CO_2 and CH_4 simulations led to an offset between the simulated values and measurements. Due to the increasing trend of CO_2 and CH_4 in the atmosphere, each spinup year (repeating year 2005) adds the yearly growth rate of 2005 to the modelled CO_2 and CH_4 values, leading to globally higher simulated values relative to the measurement. The global modelled growth of CO_2 and CH_4 in 2005 at the surface is 1.41 ppm and 0.96 ppb, respectively. In addition, for CH_4 the initial fields prior to the spinup are based on year 2010, introducing an additional offset. We quantify the overall offset by calculating the difference between the modelled CO_2 and CH_4 values used to initialize our uncoupled and coupled simulations (1st of January 2005) to measurements at different baseline NOAA GGGRN sites (Barrow, Mauna Loa, American Samoa (Tutuila) and South Pole, average value for January 2005). The resulting offset is 14 ppm for CO_2 and 45.8 ppb for CH_4. We subtract this offset from the modelled values when comparing to surface, column and aircraft measurements.

Both the column and surface measurements are impacted by data gaps. To minimize the impact of the noncontinuous measurements and inconsistent measurement time periods on the analysis, we use a consistent time period (2010–2017) when analyzing the measurement-model differences. We find the fewest data gaps during this time period; however, a few sites are still subject to missing measurements (column: Ny Alesund, Rikubetsu, Edwards, Anmyeondo, Saga, Ascension Island, Reunion; surface: Trinidad, Easter Island, Christmas Island). Due to short timeseries at the Manaus and Burgos TCCON sites, we exclude them from the plots representing the measurement-model differences in the next section (Sect. 6.1); however, the full timeseries at all sites can be found in Fig. S16–S21.

6.1 Comparison with column measurements

Figure 12 shows the differences between the modelled values (uncoupled, coupled and *coupled-origOH*) and measurements at different TCCON sites for CH_4 (a–e), CO (f–j) and CO_2 (k–o) plotted against the latitude of each site. We also show the normalized mean bias between the modelled and measured values on each plot. Mid-latitude European sites (Białystok, Bremen, Karlsruhe, Orléans and Garmisch, grouped into Other EU sites) show similar results, hence we only present their mean value. The timeseries comparison of the total CO, CO_{CH_4}, CO_2, CO_{2CO} and CH_4 mole fractions for each site can be found in Fig. S16–S18.

On a yearly scale, for all seasons the CH_4 values from the coupled simulation show noticeably better agreement with the measurements (Fig. 12a–e, indigo line) relative to the *coupled-origOH*. The *coupled-origOH* results show a positive bias with overestimated CH_4 values for all sites; however, using globally more abundant OH fields (v9-01-03) in the coupled simulation resolve this large bias. Although the coupled simulation shows better results, updating the OH fields does not resolve all the differences, and a few NH mid-latitude sites (Anmyeondo, Tsukuba, Saga) still suggest a significant bias between the modelled and measured values, pointing to either underestimated CH_4 sources or overestimated sink fields (e.g., OH). Differences in
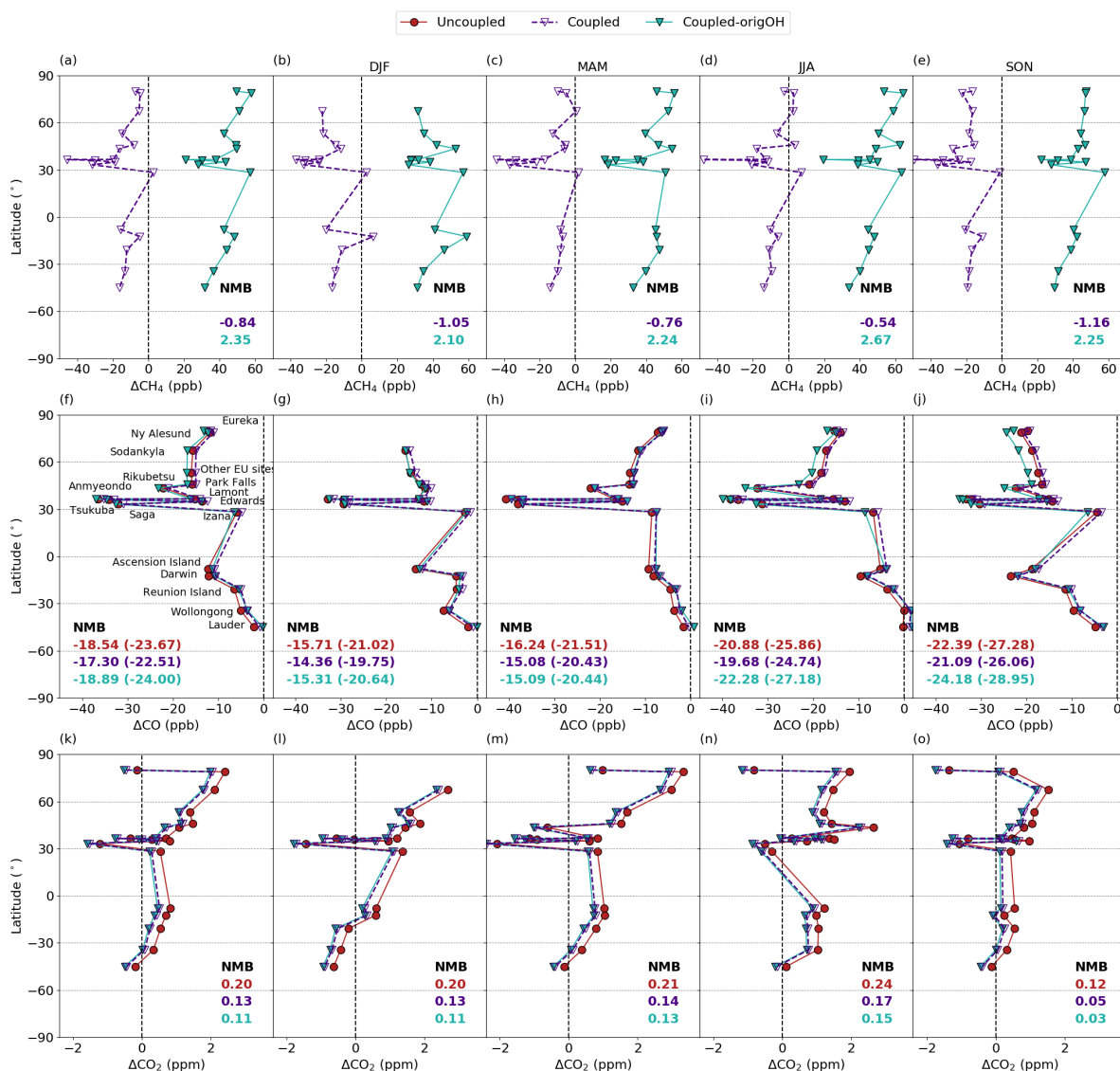
Figure 12. Column-averaged mole fraction model-measurement differences (uncoupled (red), coupled (indigo) and *coupled-origOH* (turquoise)) for CH_4 (a–e), CO (f–j) and CO_2 (k–o), as a function of latitude, averaged for 2010–2017 with annual values (a, f, k) and for different seasons: Dec–Jan–Feb (b, g, l) , March–April–May (c, h, m), June–July–Aug (d, i, n), Sept–Oct–Nov (e, j, o) . The numbers inset represent the Normalized Mean Bias (NMB). For CO we also show the NMB based on the unscaled CO values (shown in the parentheses).

the modelled-measured values throughout the seasons highlight potential contributors to the observed biases. For most SH (except Darwin during DJF) and NH mid-latitude sites (except Izana during DJF, MAM and JJA and Park Falls during JJA)

the coupled simulated values are lower relative to the measurements, with a smaller bias during SH autumn/winter (MAM,

455 JJA). In the NH polar regions we find a positive bias during NH summer (JJA) and negative bias during the other seasons. During the growing season, CH_4 permafrost emissions are released in the Arctic regions (Laurion et al., 2010); however, this emission is not included in the simulation. Adding this emission would make our simulated CH_4 values in the Arctic regions even higher during summer, suggesting that either the bias in the polar regions is driven by biases in the sink fields throughout the atmosphere or the missing permafrost signal is too weak to be detected in column measurements.

460   We find the largest CO model-measurement bias for the same NH mid-latitude sites that display a large CH_4 bias (Fig. 12f–j). The smallest bias is present at sites closest to the South Pole with increasing negative bias (i.e., underestimation of the measured values) towards the NH; however, in the NH the biases show a smaller latitudinal dependence than in the SH, presumably due to the larger differences in the CO sources between regions/sites. In both hemispheres and all seasons (except SH mid-latitude regions, Lauder and Wollongong) the coupled results show the best agreement with measurements as a result

465 of stronger CO production from CH_4. In the SH we find a stronger negative bias during spring (SON) periods, while the seasonal dependence in the NH is more variable. The largest bias relative to the measurements in the NH and SH is from the *coupled-origOH* and uncoupled simulation, respectively. Differences in the CO values are driven by differences in the CH_4 loss calculation. We find that the stronger CH_4 loss in the coupled simulation leads to better agreement with measurements, suggesting that this term was underestimated in the other simulations. Previous studies showed that CO values in the SH are

470 dominated by CH_4 and NMVOC oxidation (Zeng et al., 2015; Té et al., 2016; Fisher et al., 2017), hence underestimated secondary CO production values are potentially the origin of the remaining model-measurement bias in the SH. Moreover, the largest bias in the SH is observed during spring (SON), suggesting an additional underestimated biomass burning source, since this period aligns with the burning season in the SH. Note, due to potential errors in the TCCON column CO scaling factors we also compare our modelled CO with the unscaled column CO values that are higher by $\approx 7\%$. For all sites, we

475 obtain the unscaled values by multiplying the column CO by 1.0672. The unscaled values will further increase the negative model-measurement bias.

    For most sites and seasons, the simulated CO_2 values are higher than the measurements (Fig. 12k–o); however, a few sites in the NH tropical and polar, as well SH mid-latitude, regions show lower CO_2 values in the simulation (Anmyeondo, Saga, Eureka and Lauder based on the annual values). Not taking into account these four sites, we find a latitudinal dependence of

480 the bias, increasing from the SH polar regions towards the North Pole. In the SH, a large bias is seen during autumn/winter periods (MAM, JJA) in tropical regions, potentially driven by an underestimated terrestrial CO_2 sink in the tropics. This bias is potentially even stronger in the NH tropical regions; however, we cannot confirm this due to a lack of TCCON sites in this region. The NH mid-latitude regions show a strong bias during all seasons, with both overestimated and underestimated CO_2 values. Both the coupled and *coupled-origOH* simulations show better agreement for most sites while the uncoupled

485 simulation results show the largest bias. The main difference between the uncoupled vs coupled CO_2 values is the weaker CO_2 chemical production in the coupled simulations, suggesting that this source term might have been overestimated in the uncoupled simulation.

Overall, our coupled simulation show better agreement with column measurements (smallest model-measurement bias) than the original uncoupled simulation. The coupling improves the model-measurement offset; however, the distribution of

490 the differences between sites are consistent between different simulation versions. Further bias reductions would come from reducing uncertainties in other fluxes and transport. The inclusion of an OH-feedback between species would also impact the model-measurement bias, especially during enhanced localized emission events (i.e., fires). As an example, strong CO emissions would lead to depleted OH values, resulting in weaker oxidation of CH_4 and production of $P(CO)_{CH_4}$. This feedback is not captured in either of the simulations since the OH fields are fixed and separated between species.

495 6.2 Comparison with surface measurements

We complement the column measurements with surface measurements to highlight the impact of the chemical sources at the surface relative to the column. Figure 13 shows the differences between the measurements versus the uncoupled, coupled and *coupled-origOH* simulations at different surface sites for CH_4 (a–e), CO (f–j) and CO_2 (k–o) plotted against the latitude of each site. The timeseries comparison for each site can be found in Fig. S19–S21. Note, relative to the column results the surface

500 comparison is more strongly impacted by the coarse model resolution ($2°x2.5°$). The measured and modelled column values are more representative of regional and larger scale processes so the impact of the model resolution is weaker.

In some regions the surface model-measurement comparison show differences relative to the column comparisons, highlighting the importance of using both surface and column measurements for validation, and for identifying potential processes that drive the observed differences. Similar to the column comparison, for CH_4 the surface values from the coupled simula-

505 tion show better agreement with measurements; however, the surface CH_4 values are consistently higher (positive bias) in the simulations, while in the column results we find lower simulated CH_4 values (negative bias). This difference is potentially due to the mis-representation of CH_4 in the stratosphere that only impacts the column data or to stratospheric biases due to insufficient spin up period.

For CO, the NH biases are similar to the column comparison, with the best agreement for the coupled results. For the SH

510 the bias between the surface and column comparison differ between simulations. In contrast to the column results where, on average, the coupled shows the best agreement, at the surface we find the best agreement with the *coupled-origOH* result (followed by coupled) in SH tropical regions, and uncoupled results (followed by coupled) in the remaining SH regions. Moreover, the column CO values are lower than the measurements; however, at surface level we see an overestimation of the CO values for some SH sites, although a number of these sites is in a region where we lack column measurements. The

515 overestimated values in the SH might be partially due the weaker vertical mixing in the model leading to buildup of CO in the planetary boundary layer.

For CO_2, we find similar results between the surface and column, with overall a larger range of biases in the surface data. The strong negative bias seen at some NH sites in the column comparison is not present in the surface comparison. This difference is potentially due to the diel cycle, which is less pronounced in the column data, coupled with an incorrect flux distribution.

520 In the SH, we see a negative bias for sites between 45–90° S, a region where we lack column measurements. The differences
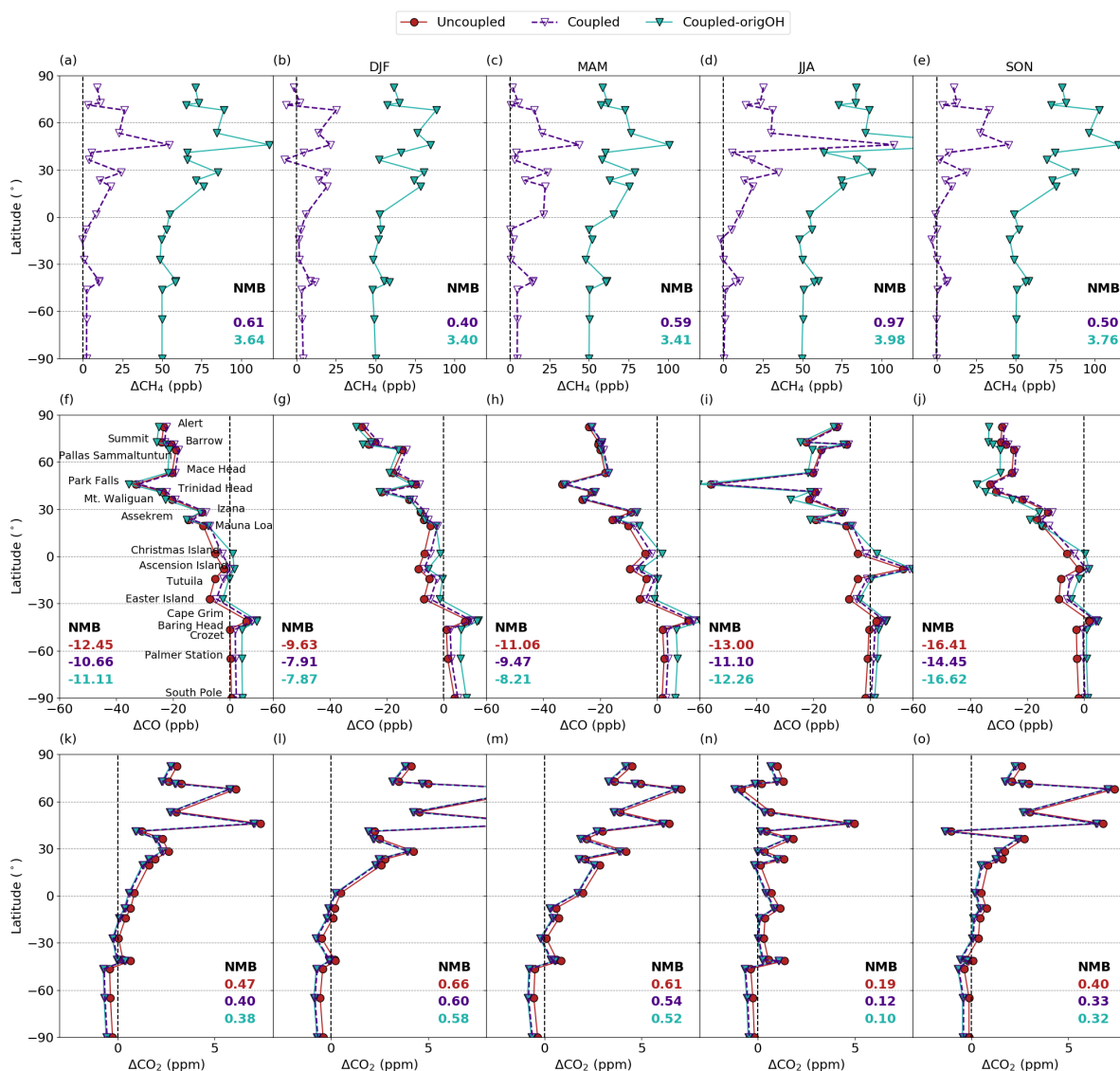
Figure 13. Surface mole fraction model-measurement differences (uncoupled (red), coupled (indigo) and *coupled-origOH* (turquoise)) for CH_4 (a–e), CO (f–j) and CO_2 (k–o), as a function of latitude, averaged for 2010–2017 with annual values (a, f, k) and for different seasons: Dec–Jan–Feb (b, g, l), March–April–May (c, h, m), June–July–Aug (d, i, n), Sept–Oct–Nov (e, j, o). The numbers inset represent the Normalized Mean Bias (NMB).

in the polar regions are potentially impacted by additional CO_2 exchange from air–sea ice interaction, a process that is not included in the simulation, and still subject to large uncertainties (Søgaard et al., 2013).

Overall, our simulation updates lead to better representation of observed CO_2, CH_4 and CO for most regions and seasons through the updated calculations of $P(CO)_{CH_4}$ and $P(CO_2)$ and through using updated OH fields. However, biases relative

525 to the measurements still remain, especially in the NH. For all three gases, we find the smallest biases in the SH, with an increasing trend towards the North Pole. Different biases in the surface and column comparison suggest that potential biases in vertical transport should also be explored.

6.3 Comparison with aircraft measurements

We further compare the simulations with aircraft measurements collected as part of ATom (campaign 1: July–August 2016,

530 2: January–February 2017, 3: September–October 2017 and 4: April–May 2018) during 2016–2018. Figure 14 shows the differences between the modelled and measured CH_4, CO and CO_2 values during the four campaigns as a function of latitude and pressure. The spatial distribution of the differences between the modelled and measured values is shown in Fig. S22.

The latitudinal change of the aircraft model-measurement differences, for all three gases and simulations follows the pattern seen in the column data. For CH_4 and CO (on average) the coupled simulation shows the closest values to measurements, with

535 lower modelled values. The negative CO bias is present during all seasons and for latitudinal bands except during ATom-2 (SH summer) and ATom-4 (SH fall) south of 50–60°. In the column data we do not have sites south of 45° and in tropical regions in the NH and cannot identify these biases. For CO_2 we find a negative bias in the SH and positive bias in the NH with similar magnitude. Both the coupled and *coupled-origOH* simulations result in almost the same CO_2 values, while the uncoupled results show the same distribution of the biases but with a consistent offset with overall better estimates in the SH

540 and larger positive bias (relative to the measurements) in the NH.

The altitudinal distribution of the model-measurement biases is similar between simulations. For CH_4 there is no significant change in the vertical distribution of the biases. Using different OH fields as before impacts the overall model-measurement bias, switching from a positive to a negative bias but it has a small impact on the vertical distribution of the biases. For CO, the coupled simulation shows better estimates during all campaigns except ATom-4 during June–July when the model-

545 measurement bias is the smallest in the *coupled-origOH* simulation. Overall, the modelled CO values underestimates the measurements during all four campaigns/seasons and vertical levels. Differences between the three simulations reduce approaching higher altitudes in the model. The vertical distribution of the CO_2 biases only differs between simulations in the offsets.

Figure 15 shows the altitude versus latitude cross-sections of the CO_2 and CO chemical tracers along the ATom flight tracks.

550 The cross-sections are constructed from linear interpolation between modelled values at the aircraft measurement locations after averaging the modelled data as described in Sect. 6.

The CO_{CH_4} values in the coupled simulation reflect the seasonal pattern in the production fields shown in Fig. 10. The mole fractions are highest in the NH during the NH summer (ATom-1) followed by NH fall (ATom-3). During NH winter (ATom-2), we see a shift of the production from the Northern to the Southern Hemisphere while during NH spring (ATom-4) we find high

555 mole fraction values in the tropical regions. The uncoupled simulation shows a similar distribution but with lower values, while the *coupled-origOH* shows higher values in the SH and lower values in the NH during all campaigns except ATom-4.
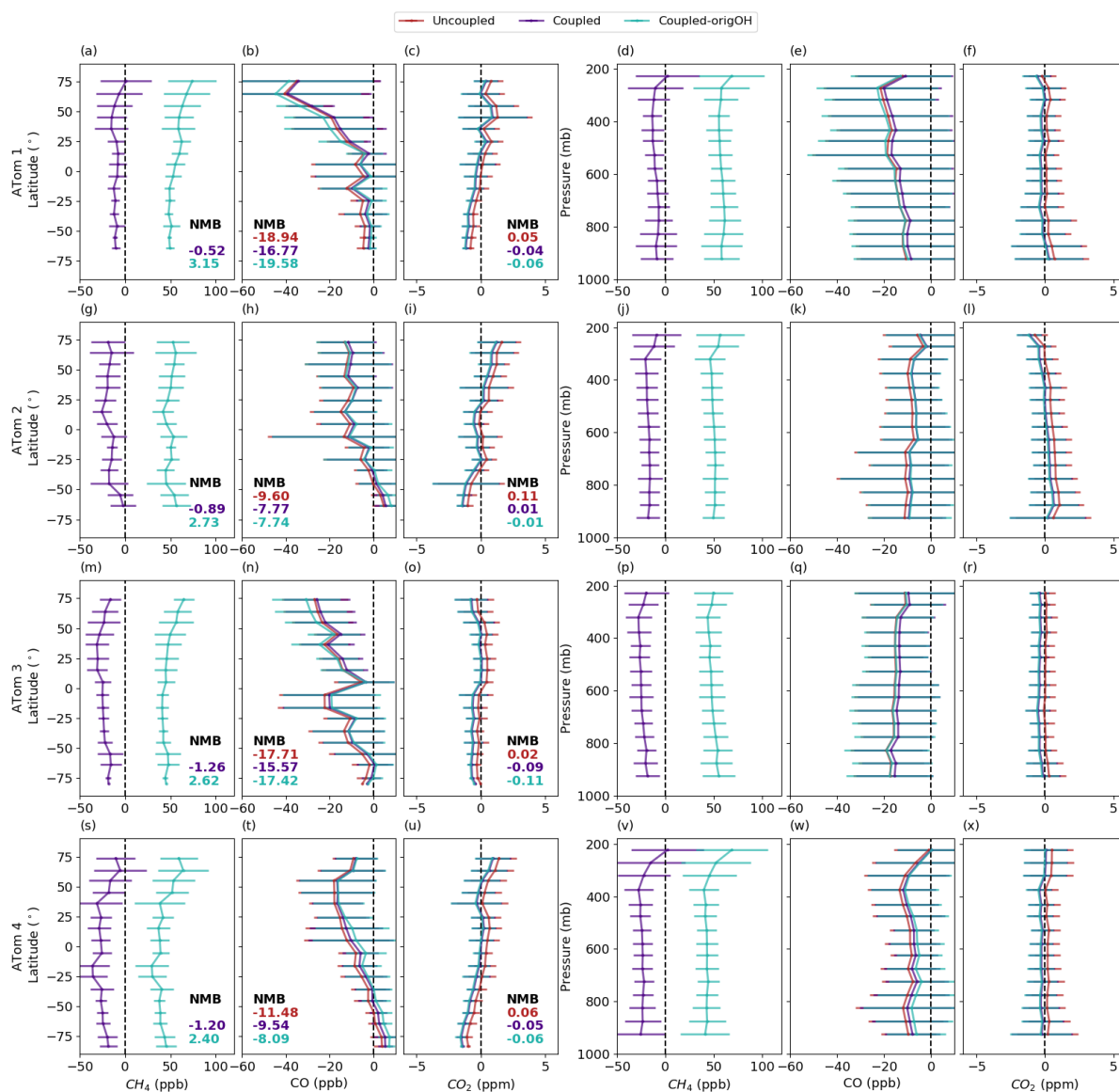
Figure 14. Aircraft model-measurement (uncoupled (red), coupled (indigo) and *coupled-origOH* (turquoise)) CH_4, CO and CO_2 differences, shown as their latitudinal (CH_4: a, g, m , s, CO: b, h, n, t, CO_2: c, i, o, u) and altitudinal distribution (CH_4: d, j, p, v, CO: e, k, q, w, CO_2: f, l, r, x) during the four ATom campaigns in June–July 2016 (a–f), Dec–Jan 2017 (g–l), Aug–Sep 2017 (m–r) and Mar–Apr 2018 (s–x). Horizontal lines show standard deviation within each bin. The data is averaged into 10° latitudinal and 50 mb pressure bins. The numbers inset represent the Normalized Mean Bias (NMB).
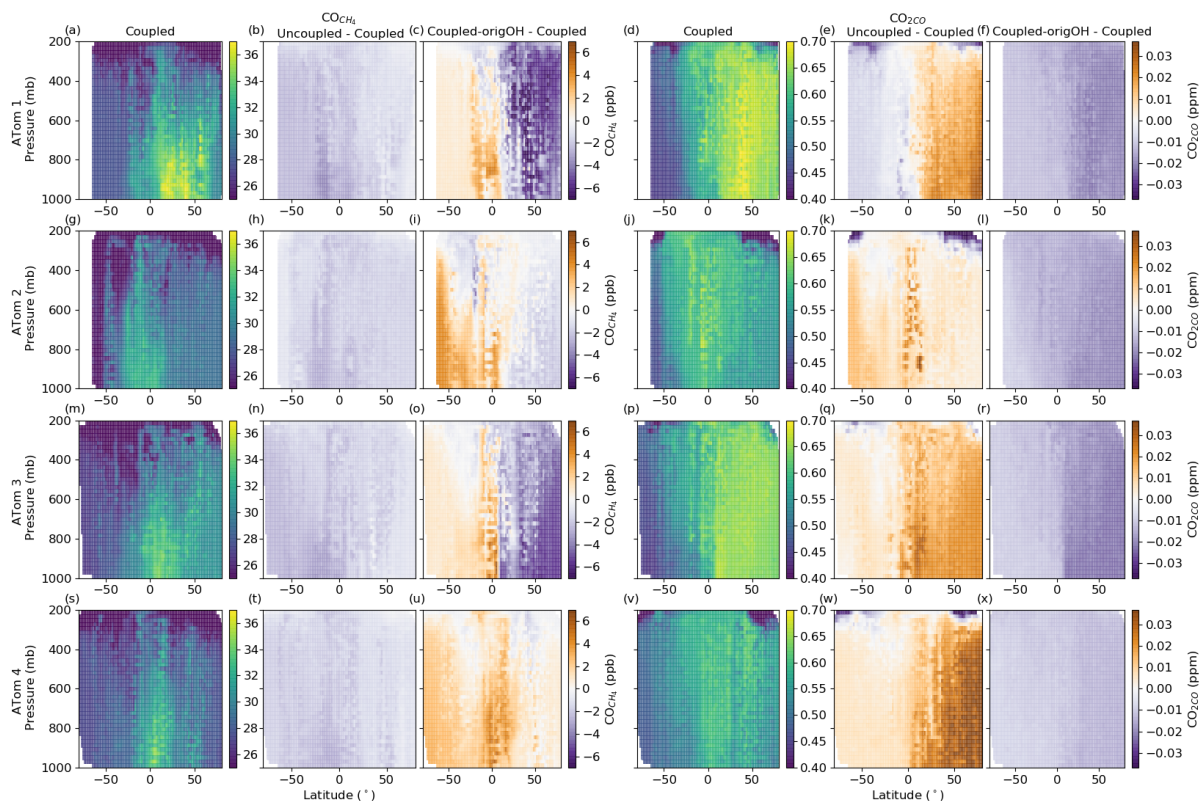
Figure 15. Altitude versus latitude cross-sections of chemically produced CO (CO_{CH_4}, a–c, g–i, m–o, s–u) and CO_2 (CO_{2CO}, d–f, j–l, p–r, v–x) mole fractions from the coupled simulation along with the uncoupled and *coupled-origOH* differences relative to the coupled simulation during the 4 ATom campaigns.

The modelled CO_{2CO} values are more mixed throughout the atmosphere. As with CO_{CH_4}, we observe the highest CO_{2CO} values in the NH during NH summer followed by NH fall. In the SH, CO_{2CO} is highest during SH summer (ATom-2) but not as high as the NH summer values in the NH. The *coupled-origOH* simulation shows a similar distribution but with lower

560 values, while the uncoupled simulation points to overall higher values globally except during June–July (ATom-1) when the mole fractions are lower in the SH. As shown in Fig. 14, the differences in the chemical fields between simulations are also reflected in the total values of CO and CO_2.

7   Conclusions

We developed a coupled carbon greenhouse gas simulation in the GEOS-Chem chemical transport model that combines CO_2,

565 CH_4 and CO, through their chemical dependence. The coupling between the three gases is from the chemical production of CO from CH_4 loss fields ($P(CO)_{CH_4}$) and the chemical production of CO_2 from the oxidation of CO ($P(CO_2)$). In the

previous uncoupled version of these simulations, the chemical productions were handled offline based on monthly archived fields for specific years from older model versions, while in our coupled simulation we calculate $P(CO)_{CH_4}$ and $P(CO_2)$ at every model timestep.

570   Along with the uncoupled versions of CO_2, CH_4 and CO simulations, we run two versions of the coupled simulation using (i) updated and consistent OH fields (v9-01-03) for the calculation of CH_4 and CO loss (coupled) and (ii) using disconnected OH fields (v5-07-08) for the calculation of CH_4 loss to match the OH used in the original uncoupled simulation (*coupled-origOH*). We compare the uncoupled and coupled results to identify the impact of the online calculation of the chemical terms, while the *coupled-origOH* results are used to identify the impact of inconsistent OH fields between species.

575   Our budget estimates from the coupled simulation agree with known literature values. For the 2006–2017 time period our coupled results show an increase in $P(CO)_{CH_4}$ with time due to the interannual variability of CH_4 loss and a dependence on climate anomalies (i.e., El Niño Southern Oscillation). We find differences between the coupled and uncoupled simulations ranging from 29–61 Tg CO yr^{-1} (1.2–2.6 % of the total CO source in the coupled version). The stronger production in the coupled simulation is a result of using updated and globally higher OH values for the calculation of CH_4 loss. Our $P(CO_2)$

580   from the coupled simulations are weaker than in the uncoupled simulation, with a 0.04–0.09 Pg C yr^{-1} difference (0.3–0.7 % of the total CO_2 source in the coupled version) but with stronger production in tropical land regions.

We find the choice of the OH fields between simulations and species has a significant impact on the differences in the chemical terms and resulting mole fractions. Globally, the $P(CO)_{CH_4}$ fields are significantly different between the coupled and *coupled-origOH* simulations due to different OH fields, leading to large differences in the modelled mole fractions of the

585   chemical tracers. However, the choice of OH field when calculating the CH_4 loss has a negligible impact on $P(CO_2)$ since it only represents an indirect and minor contribution when calculating $P(CO_2)$

Our CH_4, CO and CO_2 values from the coupled simulation overall show better agreement with all three measurement products we use for the validation (TCCON column measurements, NOAA GGGRN surface measurements and ATom aircraft data). The exception are tropical surface sites in the SH and sites between 40–90° S, where the *coupled-origOH* and uncoupled

590   CO values show better agreement, respectively. The uncoupled simulation also shows better agreement for surface CO_2 in the 45–90° S region, as well in the SH when comparing to aircraft data. These findings point to further biases that were previously masked when using only the uncoupled simulation through the limited simulation of the chemical terms.

Based on the model-measurement biases we find that the default v5-07-08 OH fields were incorrect when calculating the CH_4 loss. Increasing the OH concentrations with a seasonality of maximum surface value in May improves both our CH_4 and

595   CO modelled values. For CO, the biases in the SH can partially be explained by underestimated biomass burning emissions, especially during the dry season, and underestimated secondary CO production (CH_4 and NMVOC oxidation) values. Our coupled simulation suggests that the chemical production of CO_2 in the Amazon was significantly underestimated in previous $P(CO_2)$ studies (Nassar et al., 2010). We overall find stronger $P(CO_2)$ above tropical land regions. South America, Central Africa and northern Australia are characterized by strong biomass burning and our coupled model simulates the $P(CO_2)$

600   in these regions during the fire season to be stronger than in previous fields, while the stronger $P(CO_2)$ in regions such as East Asia and North America points to enhanced anthropogenic CO emissions. For CO_2 inclusion of the missing exchange

from air–sea ice interaction can potentially contribute to better modelled values in the polar regions. Differences in the model-measurement biases between the column and surface data also point to the mis-representation of CH_4 in the stratosphere and biases in the vertical mixing that impacts all three gases. Excluding the OH feedback can also lead to persistent biases in the

605   modelled values, especially in regions where chemical production/loss is enhanced.

The newly developed coupled simulation enables future investigations of the co-variations of CO_2, CH_4 and CO, as well as their interannual variability, that will provide better understanding of their interactions. We have shown that coupling the three gases result in more accurate modelled values and improves our ability to identify source and sink fields that are over- or underestimated in the model. Although our updates include better model-measurement agreement for all three gases, biases

610   still remain, highlighting the importance of further improvement of these simulations. These differences are heavily influenced by the existing uncertainties in variety of carbon gas sources and sinks (Dlugokencky et al., 2011; Bukosa et al., 2019; Bastos et al., 2020). The new coupled simulation paves the way for future improvements, including inclusion of a CH_4–OH–CO feedback and implementation into the GEOS-Chem Adjoint used for inverse modelling, that will further improve our ability to constrain the fluxes of the carbon gases. With updates such as this simulation we will be able to better highlight and identify

615   the origin of the model-measurement differences and constrain the sources, sinks and budgets of CO_2, CH_4 and CO, crucial for future climate projections and mitigation policies.

Appendix A: Appendix A

Geoscientific
Model Development
Discussions

Table A1. Column and surface stations used for the coupled simulation validation. Sites are ordered based on latitude, from highest to lowest.

Station	Latitude	Longitude	Elevation (m)
TCCON sites			
Eureka[a]	80.05° N	86.42° W	610
Ny Alesund[b]	78.90° N	11.89° E	20
Sodankyla[c]	67.37° N	26.63° E	188
Białystok[d]	53.23° N	23.02° E	180
Bremen[e]	53.10° N	8.85° E	27
Karlsruhe[f]	49.10° N	8.43° E	116
Orléans[g]	47.97° N	2.11° E	130
Garmisch[h]	47.48° N	11.06° E	740
Rikubetsu[i]	43.46° N	143.77° E	380
Lamont[j]	36.60° N	97.49° W	320
Anmyeondo[k]	36.54° N	126.33° E	30
Tsukuba[l]	36.05° N	140.12° E	30
Edwards[m]	34.96° N	117.88° W	699
Saga[n]	33.24° N	130.29° E	7
Burgos[o]	18.53° N	120.62° E	35
Manaus[p]	3.21° S	60.60° W	50
Darwin[q]	12.43° S	130.89° E	30
Reunion Island[r]	20.90° S	55.48° E	87
Wollongong[s]	34.41° S	150.88° E	30
Lauder[t]	45.04° S	169.68° E	370
Both TCCON sites and surface[x,y,z]			
Park Falls[u]	45.94° N	90.27° W	440
Izana[v]	28.30° N	16.50° W	2370
Ascension Island[w]	7.91° S	14.33° W	10
Surface sites[x,y,z]			
Alert	82.45° N	62.51° W	185
Summit	72.50° N	38.42° W	3209
Barrow	71.32° N	156.61° W	11
Pallas Sammaltunturi	67.97° N	24.12° E	565
Mace Head	53.33° N	9.89° W	5
Trinidad Head	41.06° N	124.15° W	107
Mt. Waliguan	36.29° N	100.89° E	3810
Assekrem	23.26° N	5.63° E	2710
Mauna Loa	19.53° N	155.58° W	3397
Christmas Island	1.70° N	157.15° W	0
Tutuila	14.25° S	170.56° W	42
Easter Island	27.16° S	109.43° W	47
Cape Grim	40.67° S	144.69° E	94
Baring Head	41.41° S	174.87° E	85
Crozet	46.43° S	51.84° E	197
Palmer Station	64.77° S	64.05° W	10
South Pole	89.98° S	24.80° W	2810

[a] Strong et al. (2019) [b] Notholt et al. (2019b) [c] Kivi et al. (2014) [d] Deutscher et al. (2015) [e] Notholt et al. (2019a) [f] Hase et al. (2015) [g] Warneke et al. (2014) [h] Sussmann and Rettinger (2018) [i] Morino et al. (2018c) [j] Wennberg et al. (2016) [k] Goo et al. (2014) [l] Morino et al. (2018a) [m] Iraci et al. (2016) [n] Kawakami et al. (2014) [o] Morino et al. (2018b) [p] Dubey et al. (2014) [q] Griffith et al. (2014a) [r] De Mazière et al. (2017) [s] Griffith et al. (2014b) [t] Sherlock et al. (2014) [u] Wennberg et al. (2017) [v] Blumenstock et al. (2017) [w] Feist et al. (2014) [x] CO_2: Dlugokencky et al. (2020b) [y] CH_4: Dlugokencky et al. (2020a) [z] CO: Petron et al. (2020)

620

Author contributions. BB developed the code for the coupled the GEOS-Chem simulation, ran the model, performed the analysis and led the writing of the paper under the supervision and guidance of NMD and JAF. DBAJ helped formulating the method for the coupled simulation. All authors contributed to editing and revising the paper.

625

Competing interests. The authors declare that they have no conflict of interest.

630

635

Geoscientific
Model Development
Discussions

References

Allen, D., Pickering, K., Duncan, B., and Damon, M.: Impact of lightning NO emissions on North American photochemistry as determined using the Global Modeling Initiative (GMI) model, Journal of Geophysical Research: Atmospheres, 115, https://doi.org/10.1029/2010JD014062, 2010.

640 Arellano Jr., A. F. and Hess, P. G.: Sensitivity of top-down estimates of CO sources to GCTM transport, Geophysical Research Letters, 33, https://doi.org/10.1029/2006GL027371, 2006.

Bastos, A., O'Sullivan, M., Ciais, P., Makowski, D., Sitch, S., Friedlingstein, P., Chevallier, F., Rödenbeck, C., Pongratz, J., Luijkx, I. T., Patra, P. K., Peylin, P., Canadell, J. G., Lauerwald, R., Li, W., Smith, N. E., Peters, W., Goll, D. S., Jain, A., Kato, E., Lienert, S., Lombardozzi, D. L., Haverd, V., Nabel, J. E. M. S., Poulter, B., Tian, H., Walker, A. P., and Zaehle, S.: Sources of Uncertainty in Regional and Global

645 Terrestrial CO_2 Exchange Estimates, Global Biogeochemical Cycles, 34, e2019GB006 393, https://doi.org/10.1029/2019GB006393, e2019GB006393 10.1029/2019GB006393, 2020.

Bergamaschi, P., Hein, R., Brenninkmeijer, C. A. M., and Crutzen, P. J.: Inverse modeling of the global CO cycle: 2. Inversion of 13C/12C and 18O/16O isotope ratios, Journal of Geophysical Research: Atmospheres, 105, 1929–1945, https://doi.org/10.1029/1999JD900819, 2000.

650 Blumenstock, T., Hase, f., Schneider, M., Garcia, O. E., and Sepulveda, E.: TCCON data from Izana (ES), Release GGG2014R1, TCCON data archive, hosted by CaltechDATA, https://doi.org/10.14291/tccon.ggg2014.izana01.R1, 2017.

Bousquet, P., Ciais, P., Miller, J., Dlugokencky, E., Hauglustaine, D., Prigent, C., Van der Werf, G., Peylin, P., Brunke, E.-G., Carouge, R., Langenfelds, R., Lathière, J., Papa, F., Ramonet, M., Schmidt, M., Steele, L., Tyler, S., and White, J.: Contribution of anthropogenic and natural sources to atmospheric methane variability, Nature, 443, 439–443, https://doi.org/10.1038/nature05132, 2006.

655 Bukosa, B., Deutscher, N. M., Fisher, J. A., Kubistin, D., Paton-Walsh, C., and Griffith, D. W. T.: Simultaneous shipborne measurements of CO_2, CH_4 and CO and their application to improving greenhouse-gas flux estimates in Australia, Atmospheric Chemistry and Physics, 19, 7055–7072, https://doi.org/10.5194/acp-19-7055-2019, 2019.

Burkholder, J. B., Sander, S. P., Abbatt, J., Barker, J. R., Huie, R. E., Kolb, C. E., Kurylo, M. J., Orkin, V. L., Wilmouth, D. M., and Wine, P. H.: Chemical Kinetics and Photochemical Data for Use in Atmospheric Studies, Evaluation No. 18, JPL Publication 15-10, Jet

660 Propulsion Laboratory, Pasadena, 2015.

Ciais, P., Borges, A. V., Abril, G., Meybeck, M., Folberth, G., Hauglustaine, D., and Janssens, I. A.: The impact of lateral carbon fluxes on the European carbon balance, Biogeosciences, 5, 1259–1271, https://doi.org/10.5194/bg-5-1259-2008, 2008.

Ciais, P., Sabine, C., Bala, G., Bopp, L., Brovkin, V., Canadell, J., Chhabra, A., DeFries, R., Galloway, J., Heimann, M., et al.: Carbon and other biogeochemical cycles, in: Climate Change 2013: The Physical Science Basis. Contribution of Working Group I to the Fifth

665 Assessment Report of the Intergovernmental Panel on Climate Change, pp. 465–570, Cambridge University Press, 2014.

Considine, D. B., Logan, J. A., and Olsen, M. A.: Evaluation of near-tropopause ozone distributions in the Global Modeling Initiative combined stratosphere/troposphere model with ozonesonde data, Atmospheric Chemistry and Physics, 8, 2365–2385, https://doi.org/10.5194/acp-8-2365-2008, 2008.

De Mazière, M., Sha, M. K., Desmet, F., Hermans, C., Scolas, F., Kumps, N., Metzger, J.-M., Duflot, V., and Cam-

670 mas, J.-P.: TCCON data from Reunion Island (RE), Release GGG2014R0, TCCON data archive, hosted by CaltechDATA, https://doi.org/https://doi.org/10.14291/tccon.ggg2014.reunion01.R1, 2017.

Deutscher, N. M., Sherlock, V., Mikaloff Fletcher, S. E., Griffith, D. W. T., Notholt, J., Macatangay, R., Connor, B. J., Robinson, J., Shiona, H., Velazco, V. A., Wang, Y., Wennberg, P. O., and Wunch, D.: Drivers of column-average CO_2 variability at Southern Hemispheric Total Carbon Column Observing Network sites, Atmospheric Chemistry and Physics, 14, 9883–9901, https://doi.org/10.5194/acp-14-9883-
675   2014, 2014.

Deutscher, N. M., Notholt, J., Messerschmidt, J., Weinzierl, C., Warneke, T., Petri, C., Grupe, P., and Katryn-ski, K.: TCCON data from Bialystok (PL), Release GGG2014R2, TCCON data archive, hosted by CaltechDATA, https://doi.org/10.14291/tccon.ggg2014.bialystok01.R2, 2015.

Dlugokencky, E. J., Nisbet, E. G., Fisher, R., and Lowry, D.: Global atmospheric methane: budget, changes and dan-
680   gers, Philosophical Transactions of the Royal Society A: Mathematical, Physical and Engineering Sciences, 369, 2058–2072, https://doi.org/10.1098/rsta.2010.0341, 2011.

Dlugokencky, E. J., Crotwell, A. M., Mund, J. W., Crotwell, M. J., and Thoning, K. W.: Atmospheric Methane Dry Air Mole Fractions from the NOAA GML Carbon Cycle Cooperative Global Air Sampling Network, 1983-2019, Version: 2020-07, https://doi.org/https://doi.org/10.15138/VNCZ-M766, 2020a.

685 Dlugokencky, E. J., Mund, J. W., Crotwell, A. M., Crotwell, M. J., and Thoning, K. W.: Atmospheric Carbon Dioxide Dry Air Mole Fractions from the NOAA GML Carbon Cycle Cooperative Global Air Sampling Network, 1968-2019, Version: 2020-07, https://doi.org/https://doi.org/10.15138/wkgj-f215, 2020b.

Dubey, M., Henderson, B., Green, D., Butterfield, Z., Keppel-Aleks, G., Allen, N., Blavier, J.-F., Roehl, C., Wunch, D., and Lindenmaier, R.: TCCON data from Manaus (BR), Release GGG2014R0, TCCON data archive, hosted by CaltechDATA,
690   https://doi.org/10.14291/tccon.ggg2014.manaus01.R0/1149274, 2014.

Duncan, B. N., Logan, J. A., Bey, I., Megretskaia, I. A., Yantosca, R. M., Novelli, P. C., Jones, N. B., and Rinsland, C. P.: Global bud-get of CO, 1988–1997: Source estimates and validation with a global model, Journal of Geophysical Research: Atmospheres, 112, https://doi.org/10.1029/2007JD008459, 2007.

Edwards, D. P., Emmons, L. K., Gille, J. C., Chu, A., Attié, J.-L., Giglio, L., Wood, S. W., Haywood, J., Deeter, M. N., Massie, S. T., Ziskin,
695   D. C., and Drummond, J. R.: Satellite-observed pollution from Southern Hemisphere biomass burning, Journal of Geophysical Research: Atmospheres, 111, https://doi.org/10.1029/2005JD006655, 2006.

Enting, I. G. and Mansbridge, J. V.: Latitudinal distribution of sources and sinks of CO_2: results of an inversion study, Tellus B, 43, 156–170, https://doi.org/10.1034/j.1600-0889.1991.00010.x, 1991.

Feist, D. G., Arnold, S. G., John, N., and Geibel, M. C.: TCCON data from Ascension Island (SH), Release GGG2014R0, TCCON data
700   archive, hosted by CaltechDATA, https://doi.org/10.14291/tccon.ggg2014.ascension01.R0/1149285, 2014.

Fisher, J. A., Murray, L. T., Jones, D. B. A., and Deutscher, N. M.: Improved method for linear carbon monoxide simulation and source attribution in atmospheric chemistry models illustrated using GEOS-Chem v9, Geoscientific Model Development Discussions, 2017, 1–24, https://doi.org/10.5194/gmd-2017-94, 2017.

Folberth, G., Hauglustaine, D. A., Ciais, P., and Lathière, J.: On the role of atmospheric chemistry in the global CO_2 budget, Geophysical
705   Research Letters, 32, https://doi.org/10.1029/2004GL021812, 2005.

Goo, T.-Y., Oh, Y.-S., and Velazco, V. A.: TCCON data from Anmeyondo (KR), Release GGG2014R0, TCCON data archive, hosted by CaltechDATA, https://doi.org/10.14291/tccon.ggg2014.anmeyondo01.R0/1149284, 2014.

Griffith, D. W., Deutscher, N. M., Velazco, V. A., Wennberg, P. O., Yavin, Y., Aleks, G. K., Washenfelder, R. a., Toon, G. C., Blavier, J.-F., Murphy, C., Jones, N., Kettlewell, G., Connor, B. J., Macatangay, R., Roehl, C., Ryczek, M., Glowacki, J., Cul-

710   gan, T., and Bryant, G.: TCCON data from Darwin (AU), Release GGG2014R0, TCCON data archive, hosted by CaltechDATA, https://doi.org/10.14291/tccon.ggg2014.darwin01.R0/1149290, 2014a.

Griffith, D. W., Velazco, V. A., Deutscher, N. M., Murphy, C., Jones, N., Wilson, S., Macatangay, R., Kettlewell, G., Buchholz, R. R., and Riggenbach, M.: TCCON data from Wollongong (AU), Release GGG2014R0, TCCON data archive, hosted by CaltechDATA, https://doi.org/10.14291/tccon.ggg2014.wollongong01.R0/1149291, 2014b.

715   Hase, F., Blumenstock, T., Dohe, S., Gross, J., and Kiel, M.: TCCON data from Karlsruhe (DE), Release GGG2014R1, TCCON data archive, hosted by CaltechDATA, https://doi.org/10.14291/tccon.ggg2014.karlsruhe01.R1/1182416, 2015.

Hodson, E. L., Poulter, B., Zimmermann, N. E., Prigent, C., and Kaplan, J. O.: The El Niño–Southern Oscillation and wetland methane interannual variability, Geophysical Research Letters, 38, https://doi.org/10.1029/2011GL046861, 2011.

Holloway, T., Levy II, H., and Kasibhatla, P.: Global distribution of carbon monoxide, Journal of Geophysical Research: Atmospheres, 105, 720   12 123–12 147, https://doi.org/10.1029/1999JD901173, 2000.

Holmes, C. D.: Methane Feedback on Atmospheric Chemistry: Methods, Models, and Mechanisms, Journal of Advances in Modeling Earth Systems, 10, 1087–1099, https://doi.org/10.1002/2017MS001196, 2018.

Iraci, L. T., Podolske, J., Hillyard, P. W., Roehl, C., Wennberg, P. O., Blavier, J.-F., Allen, N., Wunch, D., Osterman, G. B., and Albertson, R.: TCCON data from Edwards (US), Release GGG2014R1, TCCON data archive, hosted by CaltechDATA, 725   https://doi.org/10.14291/tccon.ggg2014.edwards01.R1/1255068, 2016.

Isaksen, I. S. and Hov, Ø.: Calculation of trends in the tropospheric concentration of O_3, OH, CO, CH_4 and NO_x, Tellus B, 39B, 271–285, https://doi.org/10.1111/j.1600-0889.1987.tb00099.x, 1987.

Jacob, D. J.: Introduction to atmospheric chemistry, Princeton University Press, 1999.

Kawakami, S., Ohyama, H., Arai, K., Okumura, H., Taura, C., Fukamachi, T., and Sakashita, M.: TCCON data from Saga (JP), Release 730   GGG2014R0, TCCON data archive, hosted by CaltechDATA, https://doi.org/10.14291/tccon.ggg2014.saga01.R0/1149283, 2014.

Kivi, R., Heikkinen, P., and Kyrö, E.: TCCON data from Sodankyla (FI), Release GGG2014R0, TCCON data archive, hosted by CaltechDATA, https://doi.org/10.14291/tccon.ggg2014.sodankyla01.R0/1149280, 2014.

Laurion, I., Vincent, W. F., MacIntyre, S., Retamal, L., Dupont, C., Francus, P., and Pienitz, R.: Variability in greenhouse gas emissions from permafrost thaw ponds, Limnology and Oceanography, 55, 115–133, https://doi.org/10.4319/lo.2010.55.1.0115, 2010.

735   Le Quéré, C., Andrew, R. M., Friedlingstein, P., Sitch, S., Hauck, J., Pongratz, J., Pickers, P. A., Korsbakken, J. I., Peters, G. P., Canadell, J. G., Arneth, A., Arora, V. K., Barbero, L., Bastos, A., Bopp, L., Chevallier, F., Chini, L. P., Ciais, P., Doney, S. C., Gkritzalis, T., Goll, D. S., Harris, I., Haverd, V., Hoffman, F. M., Hoppema, M., Houghton, R. A., Hurtt, G., Ilyina, T., Jain, A. K., Johannessen, T., Jones, C. D., Kato, E., Keeling, R. F., Goldewijk, K. K., Landschützer, P., Lefèvre, N., Lienert, S., Liu, Z., Lombardozzi, D., Metzl, N., Munro, D. R., Nabel, J. E. M. S., Nakaoka, S., Neill, C., Olsen, A., Ono, T., Patra, P., Peregon, A., Peters, W., Peylin, P., Pfeil, B., Pierrot, D., 740   Poulter, B., Rehder, G., Resplandy, L., Robertson, E., Rocher, M., Rödenbeck, C., Schuster, U., Schwinger, J., Séférian, R., Skjelvan, I., Steinhoff, T., Sutton, A., Tans, P. P., Tian, H., Tilbrook, B., Tubiello, F. N., van der Laan-Luijkx, I. T., van der Werf, G. R., Viovy, N., Walker, A. P., Wiltshire, A. J., Wright, R., Zaehle, S., and Zheng, B.: Global Carbon Budget 2018, Earth System Science Data, 10, 2141–2194, https://doi.org/10.5194/essd-10-2141-2018, 2018.

Liu, J., Bowman, K. W., Schimel, D. S., Parazoo, N. C., Jiang, Z., Lee, M., Bloom, A. A., Wunch, D., Frankenberg, C., Sun, Y., O'Dell, C. W., 745   Gurney, K. R., Menemenlis, D., Gierach, M., Crisp, D., and Eldering, A.: Contrasting carbon cycle responses of the tropical continents to the 2015–2016 El Niño, Science, 358, https://doi.org/10.1126/science.aam5690, 2017.

Logan, J. A., Prather, M. J., Wofsy, S. C., and McElroy, M. B.: Tropospheric chemistry: A global perspective, Journal of Geophysical Research: Oceans, 86, 7210–7254, https://doi.org/10.1029/JC086iC08p07210, 1981.

Maasakkers, J. D., Jacob, D. J., Sulprizio, M. P., Scarpelli, T. R., Nesser, H., Sheng, J.-X., Zhang, Y., Hersher, M., Bloom, A. A., Bowman,
750   K. W., Worden, J. R., Janssens-Maenhout, G., and Parker, R. J.: Global distribution of methane emissions, emission trends, and OH concentrations and trends inferred from an inversion of GOSAT satellite data for 2010–2015, Atmospheric Chemistry and Physics, 19, 7859–7881, https://doi.org/10.5194/acp-19-7859-2019, 2019.

Manning, M. R., Brenninkmeijer, C. A. M., and Allan, W.: Atmospheric carbon monoxide budget of the southern hemisphere: Implications of 13C/12C measurements, Journal of Geophysical Research: Atmospheres, 102, 10 673–10 682, https://doi.org/10.1029/96JD02743.

755 Morino, I., Matsuzaki, T., and Shishime, A.: TCCON data from Tsukuba (JP), 125HR, Release GGG2014R2, TCCON data archive, hosted by CaltechDATA, https://doi.org/10.14291/tccon.ggg2014.tsukuba02.R2, 2018a.

Morino, I., Velazco, V. A., Akihiro, H., Osamu, U., and Griffith, D. W. T.: TCCON data from Burgos, Ilocos Norte (PH), Release GGG2014.R0, TCCON data archive, hosted by CaltechDATA, https://doi.org/10.14291/tccon.ggg2014.burgos01.R0, 2018b.

Morino, I., Yokozeki, N., Matzuzaki, T., and Horikawa, M.: TCCON data from Rikubetsu (JP), Release GGG2014R2, TCCON data archive,
760   hosted by CaltechDATA, https://doi.org/10.14291/tccon.ggg2014.rikubetsu01.R2, 2018c.

Murray, L. T., Jacob, D. J., Logan, J. A., Hudman, R. C., and Koshak, W. J.: Optimized regional and interannual variability of lightning in a global chemical transport model constrained by LIS/OTD satellite data, Journal of Geophysical Research: Atmospheres, 117, https://doi.org/10.1029/2012JD017934, 2012.

Nassar, R., Jones, D. B. A., Suntharalingam, P., Chen, J. M., Andres, R. J., Wecht, K. J., Yantosca, R. M., Kulawik, S. S., Bowman, K. W.,
765   Worden, J. R., Machida, T., and Matsueda, H.: Modeling global atmospheric CO_2 with improved emission inventories and CO_2 production from the oxidation of other carbon species, Geoscientific Model Development, 3, 689–716, https://doi.org/10.5194/gmd-3-689-2010, 2010.

Nassar, R., Napier-Linton, L., Gurney, K. R., Andres, R. J., Oda, T., Vogel, F. R., and Deng, F.: Improving the temporal and spatial distribution of CO_2 emissions from global fossil fuel emission data sets, Journal of Geophysical Research: Atmospheres, 118, 917–933,
770   https://doi.org/10.1029/2012JD018196, 2013.

Notholt, J., Petri, C., Warneke, T., Deutscher, N. M., Buschmann, M., Weinzierl, C., Macatangay, R., and Grupe, P.: TCCON data from Bremen (DE), Release GGG2014R1, TCCON data archive, hosted by CaltechDATA, https://doi.org/10.14291/tccon.ggg2014.bremen01.R1, 2019a.

Notholt, J., Schrems, O., Warneke, T., Deutscher, N. M., Weinzierl, C., Palm, M., and Buschmann, M.: TCCON
775   data from Ny Ålesund, Spitsbergen (NO), Release GGG2014R1, TCCON data archive, hosted by CaltechDATA, https://doi.org/10.14291/tccon.ggg2014.nyalesund01.R1, 2019b.

Novelli, P. C., Lang, P. M., Masarie, K. A., Hurst, D. F., Myers, R., and Elkins, J. W.: Molecular hydrogen in the troposphere: Global distribution and budget, Journal of Geophysical Research: Atmospheres, 104, 30 427–30 444, https://doi.org/10.1029/1999JD900788, 1999.

780 Pandey, S., Houweling, S., Krol, M., Aben, I., and Röckmann, T.: On the use of satellite-derived $CH_4 : CO_2$ columns in a joint inversion of CH_4 and CO_2 fluxes, Atmospheric Chemistry and Physics, 15, 8615–8629, https://doi.org/10.5194/acp-15-8615-2015, 2015.

Park, R. J., Jacob, D. J., Field, B. D., Yantosca, R. M., and Chin, M.: Natural and transboundary pollution influences on sulfate-nitrate-ammonium aerosols in the United States: Implications for policy, Journal of Geophysical Research: Atmospheres, 109, https://doi.org/10.1029/2003JD004473.

785   Petron, G., Crotwell, A. M., Crotwell, M. J., Dlugokencky, E. J., Madronich, M., Moglia, E., Neff, D., Wolter, S., and Mund, J.: Atmospheric
Carbon Monoxide Dry Air Mole Fractions from the NOAA GML Carbon Cycle Cooperative Global Air Sampling Network, 1988-2020,
Version: 2020-08, https://doi.org/https://doi.org/10.15138/33bv-s284, 2020.

Pétron, G., Granier, C., Khattatov, B., Yudin, V., Lamarque, J.-F., Emmons, L., Gille, J., and Edwards, D. P.: Monthly CO surface sources
inventory based on the 2000–2001 MOPITT satellite data, Geophysical Research Letters, 31, https://doi.org/10.1029/2004GL020560,
790   2004.

Rowlinson, M. J., Rap, A., Arnold, S. R., Pope, R. J., Chipperfield, M. P., McNorton, J., Forster, P., Gordon, H., Pringle, K. J., Feng, W.,
Kerridge, B. J., Latter, B. L., and Siddans, R.: Impact of El Niño–Southern Oscillation on the interannual variability of methane and
tropospheric ozone, Atmospheric Chemistry and Physics, 19, 8669–8686, https://doi.org/10.5194/acp-19-8669-2019, 2019.

Schaefer, H., Smale, D., Nichol, S. E., Bromley, T. M., Brailsford, G. W., Martin, R. J., Moss, R., Englund Michel, S., and White, J. W. C.:
795   Limited impact of El Niño–Southern Oscillation on variability and growth rate of atmospheric methane, Biogeosciences, 15, 6371–6386,
https://doi.org/10.5194/bg-15-6371-2018, 2018.

Sherlock, V., Connor, B. J., Robinson, J., Shiona, H., Smale, D., and Pollard, D.: TCCON data from Lauder (NZ), 125HR, Release
GGG2014R0, TCCON data archive, hosted by CaltechDATA, https://doi.org/10.14291/tccon.ggg2014.lauder02.R0/1149298, 2014.

Shindell, D. T., Faluvegi, G., Bell, N., and Schmidt, G. A.: An emissions-based view of climate forcing by methane and tropospheric ozone,
800   Geophysical Research Letters, 32, https://doi.org/10.1029/2004GL021900, 2005.

Søgaard, D. H., Thomas, D. N., Rysgaard, S., Glud, R. N., Norman, L., Kaartokallio, H., Juul-Pedersen, T., and Geilfus, N.-X.: The
relative contributions of biological and abiotic processes to carbon dynamics in subarctic sea ice, Polar Biology, 36, 1761–1777,
https://doi.org/10.1007/s00300-013-1396-3, 2013.

Stocker, T., Qin, D., Plattner, G.-K., Tignor, M., Allen, S., Boschung, J., Nauels, A., Xia, Y., Bex, V., and Midgley, P.: IPCC, 2013: Climate
805   Change 2013: The Physical Science Basis. Contribution of Working Group I to the Fifth Assessment Report of the Intergovernmental
Panel on Climate Change, Cambridge University Press, 2014.

Strong, K., Roche, S., Franklin, J., Mendonca, J., Lutsch, E., Weaver, D., Fogal, P., Drummond, J., Batchelor, R., and
Lindenmaier, R.: TCCON data from Eureka (CA), Release GGG2014R3, TCCON data archive, hosted by CaltechDATA,
https://doi.org/0.14291/tccon.ggg2014.eureka01.R3, 2019.

810   Suntharalingam, P., Randerson, J. T., Krakauer, N., Logan, J. A., and Jacob, D. J.: Influence of reduced carbon emissions and
oxidation on the distribution of atmospheric CO_2: Implications for inversion analyses, Global Biogeochemical Cycles, 19,
https://doi.org/10.1029/2005GB002466, 2005.

Sussmann, R. and Rettinger, M.: TCCON data from Garmisch (DE), Release GGG2014R2, TCCON data archive, hosted by CaltechDATA,
https://doi.org/10.14291/tccon.ggg2014.garmisch01.R2, 2018.

815   Té, Y., Jeseck, P., Franco, B., Mahieu, E., Jones, N., Paton-Walsh, C., Griffith, D. W. T., Buchholz, R. R., Hadji-Lazaro, J., Hurtmans, D., and
Janssen, C.: Seasonal variability of surface and column carbon monoxide over the megacity Paris, high-altitude Jungfraujoch and Southern
Hemispheric Wollongong stations, Atmospheric Chemistry and Physics, 16, 10 911–10 925, https://doi.org/10.5194/acp-16-10911-2016,
2016.

Tie, X., Jim Kao, C.-Y., and Mroz, E.: Net yield of OH, CO, and O_3 from the oxidation of atmospheric methane, Atmospheric Environment.
820   Part A. General Topics, 26, 125–136, https://doi.org/10.1016/0960-1686(92)90265-M, 1992.

Wang, H., Jacob, D. J., Kopacz, M., Jones, D. B. A., Suntharalingam, P., Fisher, J. A., Nassar, R., Pawson, S., and Nielsen, J. E.: Error correlation between CO_2 and CO as constraint for CO_2 flux inversions using satellite data, Atmospheric Chemistry and Physics, 9, 7313–7323, https://doi.org/10.5194/acp-9-7313-2009, 2009.

Wang, J. S., Logan, J. A., McElroy, M. B., Duncan, B. N., Megretskaia, I. A., and Yantosca, R. M.: A 3-D model analysis of
825   the slowdown and interannual variability in the methane growth rate from 1988 to 1997, Global Biogeochemical Cycles, 18, https://doi.org/10.1029/2003GB002180, 2004.

Warneke, T., Messerschmidt, J., Notholt, J., Weinzierl, C., Deutscher, N. M., Petri, C., Grupe, P., Vuillemin, C., Truong, F., Schmidt, M., Ramonet, M., and Parmentier, E.: TCCON data from Orléans (FR), Release GGG2014R0, TCCON data archive, hosted by CaltechDATA, https://doi.org/10.14291/tccon.ggg2014.orleans01.R0/1149276, 2014.

830   Wecht, K. J., Jacob, D. J., Frankenberg, C., Jiang, Z., and Blake, D. R.: Mapping of North American methane emissions with high spatial resolution by inversion of SCIAMACHY satellite data, Journal of Geophysical Research: Atmospheres, 119, 7741–7756, https://doi.org/10.1002/2014JD021551, 2014.

Wennberg, P. O., Wunch, D., Roehl, C., Blavier, J.-F, Toon, G. C., Allen, N., Dowell, P., Teske, K., Martin, C., and Martin., J.: TCCON data from Lamont (US), Release GGG2014R1, TCCON data archive, hosted by CaltechDATA,
835   https://doi.org/10.14291/tccon.ggg2014.lamont01.R1/1255070, 2016.

Wennberg, P. O., Roehl, C., Wunch, D., Toon, G. C., Blavier, J.-F., Washenfelder, R. a., Keppel-Aleks, G., Allen, N., and Ayers, J.: TCCON data from Park Falls (US), Release GGG2014R1, TCCON data archive, hosted by CaltechDATA, https://doi.org/10.14291/tccon.ggg2014.parkfalls01.R1, 2017.

Wofsy, S., Afshar, S., Allen, H., Apel, E., Asher, E., Barletta, B., Bent, J., Bian, H., Biggs, B., Blake, D., Blake, N., Bourgeois, I., Brock,
840   C., Brune, W., Budney, J., Bui, T., Butler, A., Campuzano-Jost, P., Chang, C., Chin, M., Commane, R., Correa, G., Crounse, J., Cullis, P., Daube, B., Day, D., Dean-Day, J., Dibb, J., Digangi, J., Diskin, G., Dollner, M., Elkins, J., Erdesz, F., Fiore, A., Flynn, C., Froyd, K., Gesler, D., Hall, S., Hanisco, T., Hannun, R., Hills, A., Hintsa, E., Hoffman, A., Hornbrook, R., Huey, L., Hughes, S., Jimenez, J., Johnson, B., Katich, J., Kelling, R., Kim, M., Kupc, A., Lait, L., Lamarque, J.-F., Liu, J., McKain, K., McLaughlin, R., Meinardi, S., Miller, D., Montzka, S., Moore, F., Morgan, E., Murphy, D., Murray, L., Nault, B., Neuman, J., Newman, P., Nicely, J., Pan, X., Paplawsky, W.,
845   Peischl, J., Prather, M., Price, D., Ray, E., Reeves, J., Richardson, M., Rollins, A., Rosenlof, K., Ryerson, T., Scheuer, E., Schill, G., Schroder, J., Schwarz, J., St.Calir, J., Steenrod, S., Stephenes, B., Strode, S., Sweeney, C., Tanner, D., Teng, A., Thames, A., Thompson, C., Ullmann, K., Veres, P., Vizenor, N., Wagner, N., Watt, A., Weber, R., Weinzierl, B., Wennberg, P., Williamson, C., Wilson, J., Wolfe, G., Woods, C., and Zeng, L.: ATom: Merged Atmospheric Chemistry, Trace Gases, and Aerosols, https://doi.org/10.3334/ORNLDAAC/1581, 2018.

850   Wuebbles, D. J. and Hayhoe, K.: Atmospheric methane and global change, Earth-Science Reviews, 57, 177–210, https://doi.org/10.1016/S0012-8252(01)00062-9, 2002.

Wunch, D., Toon, G. C., Wennberg, P. O., Wofsy, S. C., Stephens, B. B., Fischer, M. L., Uchino, O., Abshire, J. B., Bernath, P., Biraud, S. C., Blavier, J.-F. L., Boone, C., Bowman, K. P., Browell, E. V., Campos, T., Connor, B. J., Daube, B. C., Deutscher, N. M., Diao, M., Elkins, J. W., Gerbig, C., Gottlieb, E., Griffith, D. W. T., Hurst, D. F., Jiménez, R., Keppel-Aleks, G., Kort, E. A., Macatangay, R., Machida, T.,
855   Matsueda, H., Moore, F., Morino, I., Park, S., Robinson, J., Roehl, C. M., Sawa, Y., Sherlock, V., Sweeney, C., Tanaka, T., and Zondlo, M. A.: Calibration of the Total Carbon Column Observing Network using aircraft profile data, Atmospheric Measurement Techniques, 3, 1351–1362, https://doi.org/10.5194/amt-3-1351-2010, 2010.

Wunch, D., Toon, G. C., Blavier, J.-F. L., Washenfelder, R. A., Notholt, J., Connor, B. J., Griffith, D. W. T., Sherlock, V., and Wennberg, P. O.: The Total Carbon Column Observing Network, Philosophical Transactions of the Royal Society A: Mathematical, Physical and

860   Engineering Sciences, 369, 2087–2112, https://doi.org/10.1098/rsta.2010.0240, 2011.

Zeng, G., Williams, J. E., Fisher, J. A., Emmons, L. K., Jones, N. B., Morgenstern, O., Robinson, J., Smale, D., Paton-Walsh, C., and Griffith, D. W. T.: Multi-model simulation of CO and HCHO in the Southern Hemisphere: comparison with observations and impact of biogenic emissions, Atmospheric Chemistry and Physics, 15, 7217–7245, https://doi.org/10.5194/acp-15-7217-2015, 2015.